UNIVERSITY OF CALIFORNIA
RIVERSIDE

Ti(III) Doped Titanium Dioxide: an Effective Strategy to Improve the Visible Light Photocatalytic Activity

A Dissertation submitted in partial satisfaction
of the requirements for the degree of

Doctor of Philosophy

in

Chemistry

by

Fan Zuo

September 2012

Dissertation Committee:

Dr. Pingyun Feng, Chairperson
Dr. Christopher A. Reed
Dr. Yadong Yin

The Dissertation of Fan Zuo is approved:

Committeee Chairperson

University of California, Riverside

Acknowledements

I would like to take this opportunity to express my sincere gratitude and respect to Professor Pingyun Feng, for her guidance and enthusiasm. I deeply appreciate her inspiring ideas, continuous support and kindly encouragement, without which, this dissertation would not have been possible. She demonstrated the dedication and rigorous attitude toward science, which will inspire and benefit me for the rest of my life.

I also thank our excellent collaborators, Prof. Christopher J. Bardeen in Department of Chemistry at UCR and his graduate student Robert J. Dillon. Prof. Bardeen and Mr. Dillon provided me the deep insight in exciton study. They helped me to characterize and analyze the decay profile of photogenerated free charge carriers.

I greatly appreciate Dr. Krassimir N. Bozhilov in Department of Earth Science at UCR for structure and morphology analysis. I also would like to thank Dr. Dan Borchardt in Department of Chemistry at UCR for the EPR training and spectra investigation, Dr Jennifer Massey for the elemental analysis in Analytical Lab at UCSB. I deeply appreciate Prof. Xianhui Bu at CSULB for his valuable suggestion, discussion and encouragement.

Over the past five years, I have also been very fortunate to have the opportunities to work together with the excellent members in Dr. Feng's group: Dr. Tao Wu, Dr. Xiang Zhao, Le Wang, Jikai Liu, Dr. Yang Hou, Dr. Zhenyu Zhang, Dr. Qipu Lin, Dr. Guiyuan

Jiang, Dr. Lei Ge, Fei Bu, Chengyu Mao, Koroush Sasan, and Phillip Smith, who help me in many ways.

I am also very grateful to the rest of my dissertation committee, Prof. Christopher A. Reed and Prof. Yadong Yin, for their valuable comments on my dissertation.

There are many others who deserve many thanks. I would like to thank the staff in Depart of Chemistry for their kindly service and help.

Finally, I want to sincerely thank my parents, my wife Sufen, my daughter Yiran, and my brother Jianqi for everything they have done for me. Without their love, encourage and support, I could not finish my Ph. D. study smoothly.

Dedication

To my wife Sufen Liu, and my daughter Yiran

ABSTRACT OF THE DISSERTATION

Ti(III) Doped Titanium Dioxide: an Effective Strategy to Improve the Visible Light Photocatalytic Activity

by

Fan Zuo

Doctor of Philosophy, Graduate Program in Chemistry
University of California, Riverside, September 2012
Dr. Pingyun Feng, Chairperson

Seeking clean and renewable energy resources has been a research focus for the past decades. Carbon-based fuel, the current primary energy resource, will be depleted in the near future. The environmental concern coming with the consumption of fossil fuel is more significant than ever. The sunlight incident on the earth's surface reaches as high as 1000W/m^2, far exceeding the human energy needs. If an efficient and environmentally benign solar energy conversion and utilization could be achieved, the energy problem will be eventually solved.

Since the first reported UV light activated photocatalyst TiO_2, many materials have been synthesized and studied for their photocatalytical activity. Among them, researchers are especially interested in those which could make H_2 from water efficiently under visible light irradiation, since the energy of visible light takes up a large proportion of

solar energy.

Herein, we investigated the Ti^{3+}-doped TiO_2 prepared by a facile one-step combustion method. It is found that Ti^{3+} extends the photoresponse of TiO_2 from the UV to the visible light region, which leads to high visible-light photocatalytic activity for the generation of hydrogen gas from water.

We further studied how the synthetic conditions such as crystallinity, surface area, particle size, crystal facets distribution and etc. affected the photocatalytic activity of the partially reduced TiO_2.

In addition, we found that the partially reduced TiO_2 with highly active facets could be fabricated by a facile hydrothermal treatment of Ti powder and hydrochloric acid. Without any additional reducing agent and surfactant, Ti^{3+} was successfully incorporated into the product, and more importantly, highly active facets developed preferentially, which is supported by the electron paramagnetic resonance (EPR) spectra and transmission electron microscopy (TEM). The as-synthesized single crystal sample showed a great improvement in the photocatalytic H_2 production activity over our previously prepared particles. It is inferred that the active facets play a crucial role for this enhancement. Measurement of the photocatalytic activity over an extended time period proved the excellent stability of the reduced TiO_2 made by this approach.

Table of Contents

List of figures

List of Tables

Chapter 1

An Overview of Photocatalysis and TiO_2 Photocatalyst

1.1 Photocatalytic Water Splitting

1.1.1 Origin of Photocatlytic Water Splitting

Energy demand for human beings is soaring every year. However, the primary energy source is still the fossil fuels, including petroleum, coal and natural gas (86.4% of all energy consumption in the world).[1] This heavy dependency on fossil fuels gives rise to two critical problems. On the one hand, the fossil fuels will be depleted in a near future. On the other hand, the release of green house gas CO_2 generated by combustion of fossil fuels impose a great impact on the environment. Hydrogen gas is broadly viewed as a sustainable and clean energy alternative for the widely used fossil-based energy, as the enthalpy of H_2 is as high as 286 KJ/mol (or 143 KJ/g, 1.3 times enthalpy of methane per unit weight), and the only product after burning is water, which makes it a ideal energy resource. In industry, commercial bulk hydrogen gas is produced by steam reforming of natural gas.

$$CH_4+H_2O \rightarrow CO+ 3H_2$$

$$CO+H_2O \rightarrow CO_2+H_2$$

These reactions are energy intensive and require high temperature (700-1000 °C). Furthermore, it consumes fossil energy and produces CO_2.

Solar energy, the radiation from the sun, has been considered as the abundant and reliable energy source. The solar energy reaching the earth in one year is much more than energy obtained from fossil fuels so far.[2] Fujishima and Honda first discovered the photocatalytic splitting of water through single crystalline TiO_2 e1ectrodes in 1972.[3] Since then, a new epoch began in the heterogeneous photocatalysis for solar energy conversion and more than 100 photocatalysts have been reported.[4] In this artificial photosynthesis process, the chemical reaction is simple:

$$H_2O \rightarrow 1/2O_2+H_2.$$

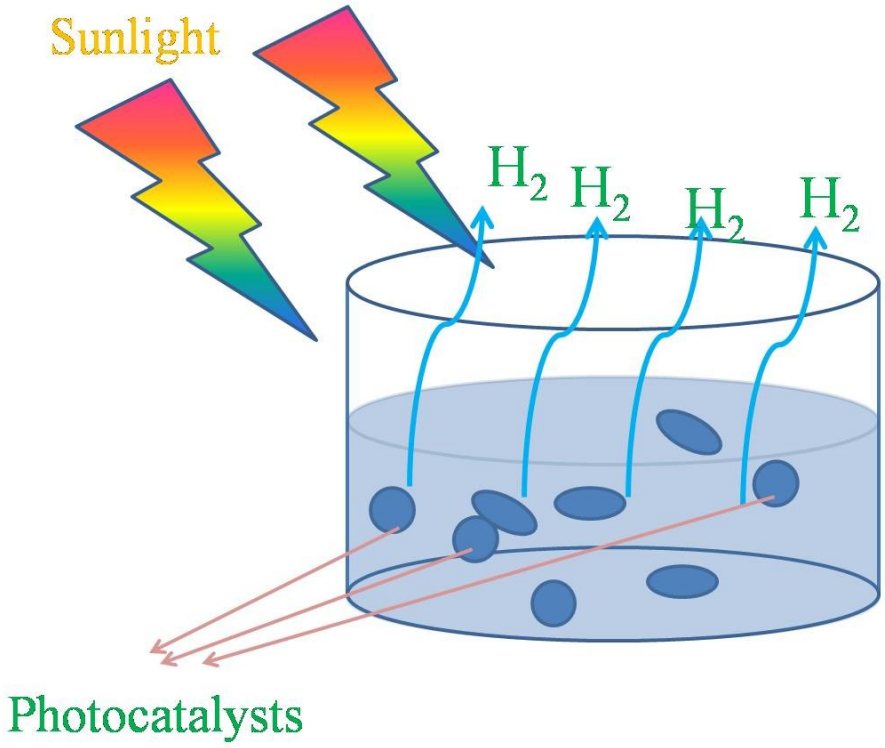

Figure 1. The scheme of the water splitting by photocatalysts.

If the H_2 gas could be produced through solar energy in a green and efficient way, the energy issue will be successfully addressed. However, water molecules are transparent and could not absorb the ultraviolet/visible (UV-Vis) light by itself. Therefore, some media are needed to absorb the solar energy and transfer it to water in some way and finally split water molecules. Semiconductors are usually used to for this purpose, and are therefore called photocatalysts. To achieve the activation of these semiconductor photocatalysts, a photon with energy exceeding the band gap needs to be absorbed, which will generate an exciton. Then the electron will be excited from the valence band into the conduction band, and a localized positive charge, which is commonly called hole, is left behind in valence band. To fulfill the water-splitting reaction, the electronic band structure of the semiconductor has to meet some requirements. First of all, for photoreduction of water, the conduction band minimum of the semiconductor must be more negative than the reduction potential of H^+/H_2, then the photogenerated electrons will transit from the conduction band minimum of semiconductor to H^+, which then will gain these electrons and be reduced to H_2. Secondly, the valence band maximum of semiconductor must more positive than the O_2/H_2O reduction potential. Then the hole left behind in the valence band will transit to water, which will be oxidized and produce O_2. For practical application, the semiconductor must be stable in aqueous solution under solar light irradiation. Most of the chalcogenide semiconductors are suffering from this

issue and will be oxidized and decomposed.[5] That is why even some very highly efficient chalcogenide materials, such as ZnS (quantum efficiency = 90%, aqueous solution under UV irradiation[6]), are not promising photocatalysts. Oxides have more chance to survive in the water splitting reaction. However, some oxides, such as ZnO, are also not stable under UV irradiation.[7] The ZnO could react with the photogenerated holes and produce Zn^{2+} and O_2.

1.1.2 Process in Photocatalytic Reaction

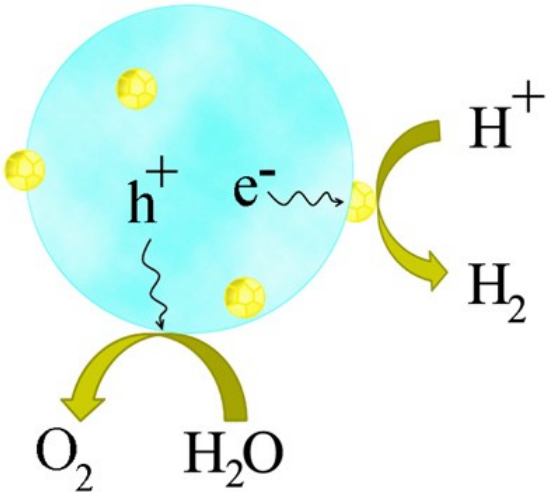

Figure 2. The process in the photocatalytic water splitting.

The primary process in photocatalytic water splitting reaction could be divided into 4 steps: 1) Photocatalyst absorbs photons to generate electron-hole pairs. Figure 2 shows the photocatalytic reactions precede on surface of semiconductor materials. The electronic band structure of semiconductors is separated into two bands, conduction band and valence band, between which is called band gap, as shown in Figure 3. When the

energy of incident photon exceeds that of a band gap, this photon will be absorbed by the semiconductor and an exciton will be formed. Then an electron will be promoted to

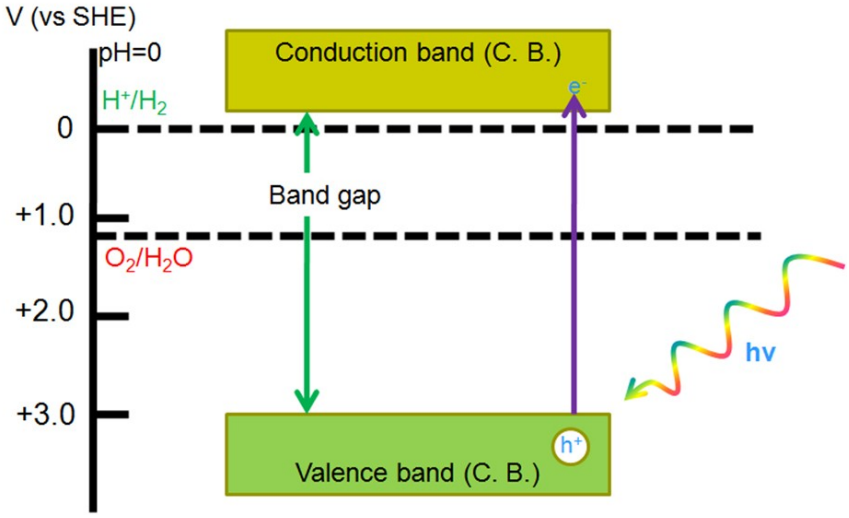

Figure 3. The procedure for photogeneration of electrons and holes.

conduction band and a hole will be left behind in valence band. Like the electrolysis, the electrons will reduce the water molecules to hydrogen gas and the holes will oxidize them to oxygen gas in overall water splitting. 2) The separation of negative charged electrons and positive charged holes and their migration to surface of the photocatalysts. Many factors greatly affect this step, including crystal structure, crystalline quality and the particle size of photocatalysts. Higher crystallinity means less structural defects in the crystal. Defects here usually play an adverse role as the recombination centers, inducing the free charge carriers, i. e. electrons and holes, to recombine with each other and convert the energy to heat (in the form of phonons) or radiation (in the form of photons), instead of splitting water into chemical fuels (in the form of H_2). The particle size is

another key point for the step 2. A small particle size means a shorter distance that photogenerated electrons and holes need to diffuse and migrate to reaction sites on the surface, greatly decreasing the possibility of recombination. 3) The surface chemical reactions. This step is highly related with the surface active sites and the surface area. Even though the as-formed free charge carriers electrons and holes are thermodynamically sufficient in potentials for water splitting, they will not achieve the goal reaction and recombine with each other if there are no active reaction sites for water splitting present on the surface. For this consideration, co-catalysts such as Pt,[8] Pd,[9] NiO,[10] RuO_2,[11] and Cr/Rh oxides[12] are broadly loaded to create active sites for H_2 evolution reaction. A similar strategy is applied for O_2 evolution. Pt[13] and Ru[14] are introduced to form active sites for this 4-electron process. Note that co-catalysts for O_2 evolution are not as common as H_2 evolution for oxide photocatalysts, and one possible explanation is the valence band for oxides is usually deep enough to oxidize water to O_2. This is a significant merit of heterogeneous photocatalysts compared to homogeneous photocatalysts, as for the latter it is a big dynamic challenge for O_2 evolution with a 4-electron process. Another consideration is blocking the back reactions of H_2 and O_2 to form water. Therefore, some research groups are trying to use other cocatalysts, such as NiO to replace the noble metals for diminishing the back reaction while assisting the water splitting reaction.[15]

Lots of photocatalysts are also good candidates for solar cells. Although both the photocatalysis and solar cell are promising strategies to utilize solar energy, there are still significant differences between them. First of all, photocatalysis converts solar energy into chemical fuels while solar cells produce electricity. Compared to electricity, chemical fuels show relative advantages in storage and transportation. Also, in the photocatalytic process, chemical reactions (oxidation and reduction) are involved, while there are no chemical reaction in solar cells. For photocatalytic water splitting, it is required all the three steps are proceed efficiently, then a high activity could be achieved. Therefore, suitable combination of electronic band structure, bulk properties, and surface characters are necessary for a high efficient photocatalyst. Also, it is expectable that good photocatalysts could be built through functionalization and modification.

1.1.3 Sacrificial O_2 and H_2 Evolution and Z- Scheme Water Splitting

As discussed before, if the photocatalysts have suitable band structure, i.e. conduction band minimum more negative than H^+/H_2 reduction potential and valence band maximum more positive than O_2/H_2O reduction potential, an overall H_2 and O_2 evolution could be obtained simultaneously in a stoichiometric ratio. However, for many semiconductors, their band structure only meets one of the above requirements, and then a sacrificial agent is usually added to the system. When a photocatalytic reaction is occurred in an aqueous solution system with a reducing reagent, or hole scavengers, such

as alcohol, sulfide or sulfite ion, the photogenerated holes will be readily consumed by these reducing reagents. Meanwhile, this process diminishes the chance of electron-hole recombination, so the electrons have more opportunity to reduce the water and produce H_2. If this strategy is combined with biomass and natural or industrial pollutant, then it will be meaningful and practical in hydrogen production. Similarly, oxidizing reagents or electron scavengers, such as Ag^+,[16] Fe^{3+},[17] Ce^{4+},[18] and etc. are commonly used in aqueous solutions to consume the photogenerated electrons and therefore boost the O_2 evolution. These half reactions with sacrificial agents are also used to evaluate if a photocatalyst satisfy the thermodynamic potentials requirement for H_2 or O_2 evolution. Note that even a photocatalyst is able to generate H_2 and O_2 in two half reactions, respectively, it does not mean that it must be able to split water molecule into H_2 and O_2 simultaneously without the assistance of sacrificial agents, due to the kinetic issue. The term "water splitting" should be exclusive used for the case that a photocatalyst absorbs the solar energy and produce both H_2 and O_2 simultaneously in a stoichiometric ratio (2:1) in absence of reducing reagents or oxidizing reagents. The overall water splitting possesses more potential for practical industrial application.

One more strategy to perform overall water splitting by some semiconductors which are only active for one of the half reactions is the Z scheme. In a Z scheme system, one semiconductor is active for H_2 evolution, and the other is active for O_2 evolution.

These two photocatalyts are combined in one system through an electron donor/acceptor pair (usually called redox shutter), such as I^-/IO_3^-.[13] In the H_2 evolution side, I^- works as an electron donor and oxidized to IO_3^-, and in the O_2 evolution side, IO_3^- works as an electron acceptor and is reduced to I^-. Viewing the whole reaction system, there is no input but solar energy, and H_2 and O_2 will be generated in stoichiometric ratio, so this Z scheme is also an overall water splitting.

1.1.4 Factors Affecting the Water Splitting Reaction and Characterization

In order to improve the efficiency of photocatalysis, the first thing is to understand what factors matter for photocatlytic process. Reviewing the three steps in the photocatalytic process, it is clear that three factors need full consideration. The first one is the sun light absorption. The more portion of sun light is absorbed by the photocatalysts, more electron-hole pairs will be generated and potentially used to split water. The solar light absorption could be studied by UV-visible light absorption measurement. The second factor is the crystallinity of the photocatalysts. The higher crystallinity means less structural defects in the crystal, and less electron-hole recombination. Usually the high crystallinity will be achieved by calcination of the products at high temperature. The crystallinity can be evaluated by the full width at half maximum (FWHM) of peaks in XRD patterns or high resolution transmission electron microscopes (HRTEM). The third factor is the surface area, which can be determined by BET measurement. Large surface

area means more reactive sites for the water reduction and oxidation reactions. To get larger surface area, we want materials are porous structure or small in particle size. However, small particle size possibly raises a quantum size effect, and causes a blue shift in the absorption spectrum and band gap widening. Sintering the photocatalysts to improve the crystallinity tend to increase the particle size and result in a decrease in surface area. The final photocatalytic activity is governed by the balance among these factors.

Also, the eventually strategies to enhance the photocatalytic activity greatly depend on the type of practical application. A high quality of crystallinity is usually preferred over a high surface area in water splitting, as in this energy uphill energy process ($\Delta G>0$), the very first concern is to prevent the recombination between photogenerated electrons and holes. On the other hand, in the organic pollutant photodecomposition process, high surface area is prior to high crystallinity, as adsorption of the organic compound is the key step.

1.2 Evaluation of Photocatalytic Water Splitting

Many strategies have been reported to synthesize various photocatalysts and to improve their activity. Before that, the first thing is how to correctly evaluate the activity among these different photocatalysts is quite important for both theoretical and practical purpose.

1.2.1 Time Course of H_2 and O_2 Evolution

The amount of H_2 and O_2 gas produced by photocatalysis need to be recorded versus the light irradiation time. The activity is reflected by the amount of gas products. Meanwhile, the stability of the photoctalysts is investigated by repeated experiments. As a long term photocatalytic reaction proceeding, no or very small activity loss is required to demonstrate the high stability for the practical use of the photocatalysts.

1.2.2 Turnover number (TON)

Like all the catalytic reactions, photocatalytic water splitting also needs to monitor the TON to prove its catalytic character. Amounts of photogenerated H_2 and O_2 need to exceed that of a photocatalyst. If the amount of gas products is less than the amount of photocatalyst, we could not confirm that this process is a photocatalytic or not, as it is possible that semiconductor self-decompose and release H_2 or O_2, which is not a real catalytic process. Turnover number is usually defined by the number of reacted molecules to that of an active site.

$$\boldsymbol{TON} = \frac{\text{number of reacted molecule}}{\text{number of active sites}}$$

However, for this heterogeneous photocatalysts system, the number of active sites is impossible to be accurately determined. Here, an alternate method is commonly used. Instead of the number of active sites, the number of molecules in a photocatalyst is used in the equation. Then a modified equation is proposed as follows:[19]

$$\boldsymbol{TON} = \frac{\text{number of reacted electrons}}{\text{number of molecules in a photocatalyts}}$$

The number of reacted electrons is calculated from the number of moles of produced H_2 or O_2 gas. The TON obtained from the above equation is underestimated than the real value according to the definition of TON due to the number of molecule in the whole photocatalyst is more than that of active sites, which are only present on the surface.

1.2.3 Quantum Yield

To assess the activity of the photocatalysts, the normalized photocatalytic activity by mass of photocatalyst is not a correct way to evaluate the activity as the photocatalytic activity is not necessarily proportional to the mass of photocatalyst. As we mentioned in the last part, the activity is determined by a balance between many factors such as the light absorption, crystallinity, and surface area. These properties do not simply comply with a linear relationship with the mass of photocatalysts. To compare the activities, the amount of photocatalyst should be kept the same in all the parallel measurements. Furthermore, if we want to compare the performance of photocatalysts from different groups, some many differences in the experimental conditions, especially the light source, make it meaningless to just consider the H_2 or O_2 evolution rate. A fair standard to assess the activity of various photocatalysts is the quantum yield (QY). The definition of quantum yield is:

$$\text{Quantum yield} = \frac{\text{number of reacted electrons}}{\text{number of absorbed photons}}$$

Unlike the H_2 or O_2 evolution rate, quantum yield excludes the disturbance from different light source. However, the number of absorbed photos is very difficult to measure. Therefore, another term called external quantum yield (or apparent quantum yield) is usually used to study the activity of the photocatalysts.[19]

$$\text{External quantum yield} = \frac{\text{number of reacted electrons}}{\text{number of incident photons}}$$

Here the number of incident photons could be determined by photo meter. The EQY is lower than the QY, as the number of absorbed photons smaller than that of incident photons due to the scattering of the solid semiconductor photocatalysts.

1.2.4 Experimental Equipment

The first equipment to study the rutile photocatalytic property was a photoelectrochemical cell. As shown in the Figure 4, it is composed by a photocathode and a photoanode. Photocathode is functioned to generate the H_2 where the water is reduced. The photoanode oxidizes water and produces O_2. Usually a third electrode is used as reference electrode. Also, these electrodes are wired to a potentiostat, which will study a series of photoelectrical properties such as I-V property and I-T property.

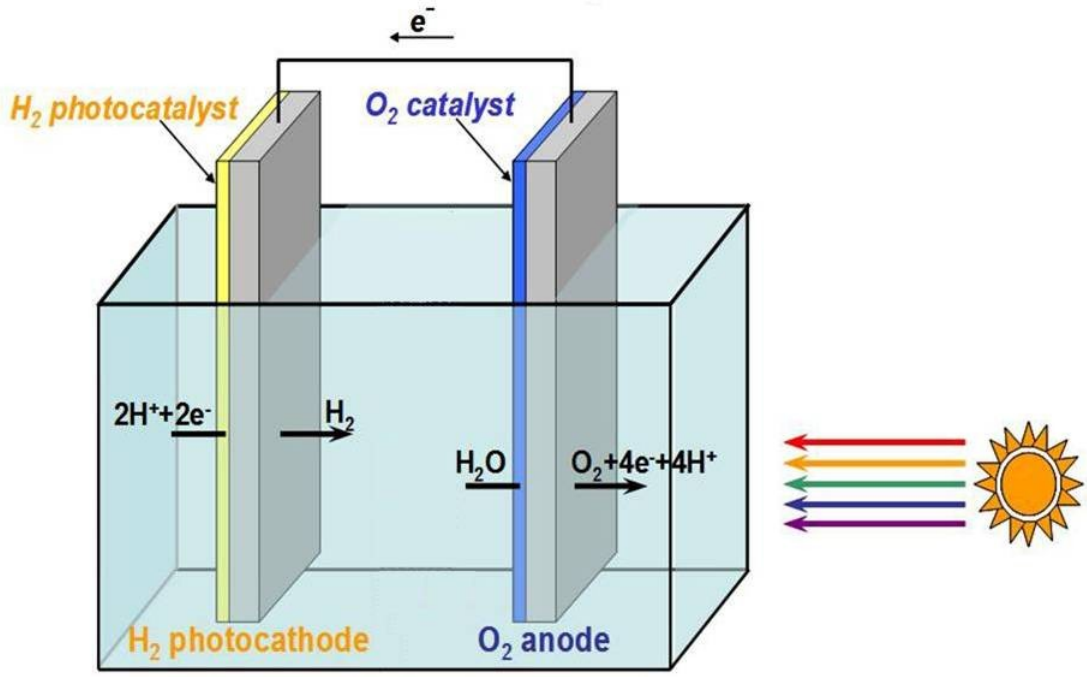

Figure 4. The scheme of the photoelectrochemical cell for water splitting.

Another commonly used apparatus for water splitting is shown in Figure 5. The water splitting reaction occurs in an air tight system. All the gas products are generated and collected in the glass tubing. The optical window for the reactor should be made of quartz to allow both the UV and visible light to go through. A circulation system is equipped to evenly distribute the products, improving the reliability and reproductivity of the data measurement. A vacuum line is connected to the reaction system for degas purpose. Completely removal of air in the reaction system to exclusion the disturbance of O_2 from air is crucial for an overall water spitting reaction. Therefore there is a critic requirement for the vacuum system and a high quality of a gas-closed reaction

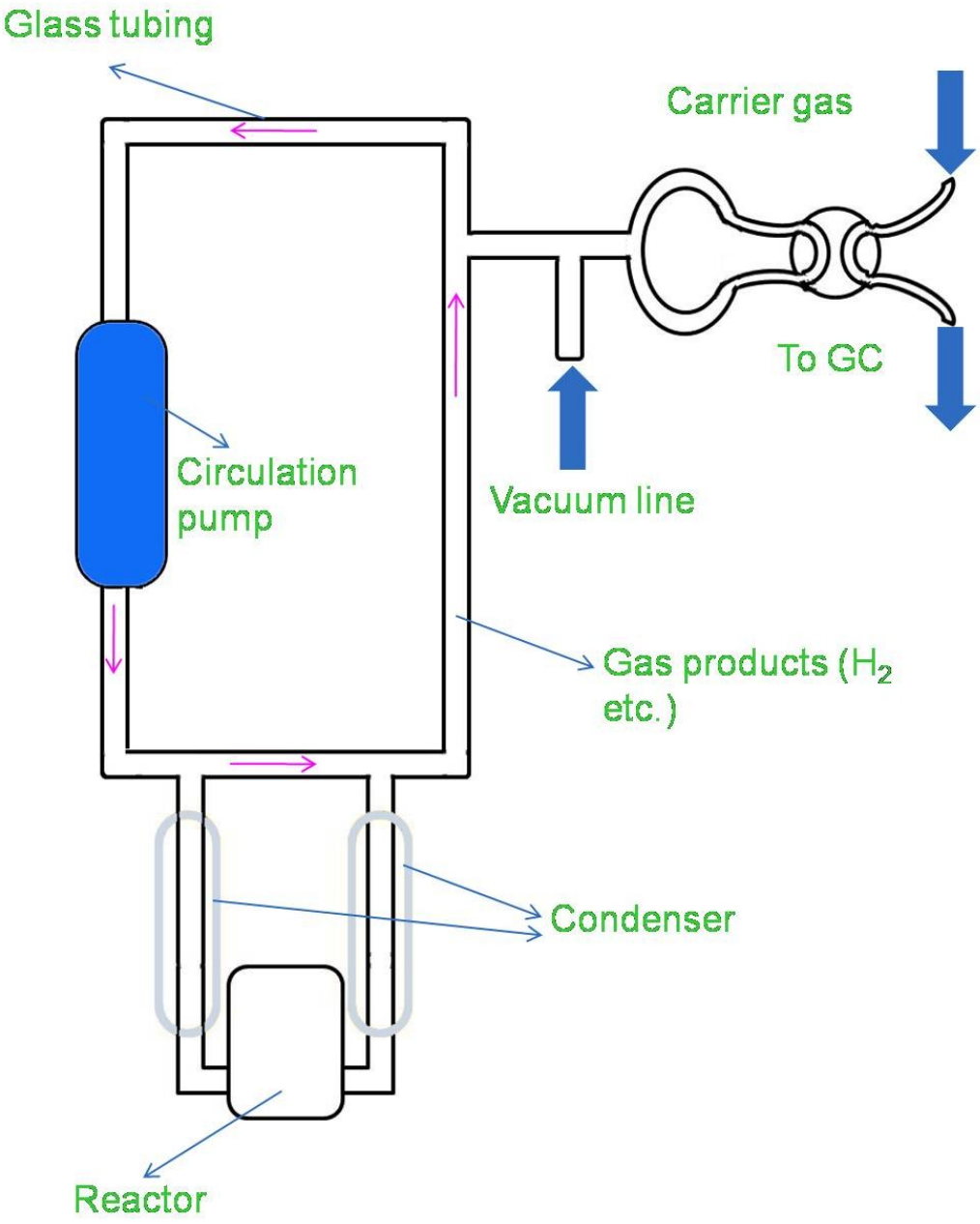

Figure 5. The scheme of setup for the photocatalytic water splitting.

system. A carrier gas line is connected to the sampling system, pushing the gas products into gas chromatography (GC). To test the H_2 and O_2, a thermal conductivity detector

(TCD) is installed in the GC. To improve the efficiency of irradiation, an inner irradiation reaction cell is recommended. Different light source is used according to different application. For a UV application, high-pressure mercury lamps are usually used. If studying the visible light activity, a Xe-lamp with various optical filters is often employed. When evaluating the solar hydrogen production, a solar simulator with an air-mass 1.5 filter (AM1.5), which will provide the power of 100 mW cm^{-2} is required.

1.3 TiO_2 Photocatalysts

To date, more than 100 photocatalysts have been reported.[4] Among these materials, TiO_2 is the first also most extensively studied materials, due to its superb merits, such as low cost, nontoxicity, high stability. Even now, it is still one of the most promising candidates for practical use.

1.3.1 TiO_2 Lattice Structure

The TiO_2 occurs in three forms in the nature, i.e. anatase phase, rutile phase, and brookite phase. All three forms of the TiO_2 include TiO_6 octahedra that are interconnected via four (Anatase), two (Rutile), or three (Brookite) shared edges and via shared corners.[20] The brookite structure is too rare to be used for experimental investigations. Both the anatase and rutile crystal structures are in distorted octahedron symmetry.[21] In rutile phase, there is a slight distortion from orthorhombic structure, where the unit cell is stretched from a cubic structure. In anatase phase, the distortion from cubic lattice is

more pronounced and thus the symmetry of anatase is lower than rutile. Also, this make the unit cell of anatase (a = 3.7845 Å, c = 9.5143 Å, 4 TiO_2 groups) is much larger than rutile (a = 4.5937 Å, c = 2.9587 Å, 2 TiO_2 groups). These differences in structures make rutile and anatase have different electronic structure and therefore different band gaps (3.15 eV for anatase and 3.0 eV for rutile).

Photocatalytic studies on brookite are rare. However, there are still some literature reporting the study of photocatalytic activity on pure brookite and mixture of TiO_2 containing brookite.[22-24] For example, Addamo et al. compared the photodecomposition activity of 2-propanol among anatase, rutile and brookite, and they pointed out that the brookite TiO_2 showed a comparable activity to that of anatase TiO_2 when they have the similar particle sizes.[25]

The surface structure is a crucial factor for the photocatalytic properties, as all the reactions occur on the surface. For TiO_2, Most surface structure studies for photochemistry have been focus on the single crystalline rutile surface partially due to the anatase single crystals are very difficult to prepare, so surface science investigations on anatase are very limited.[26] Detailed study of the surface structure for brookite is also rare (if any), as the availability of single crystal samples or high quality epitaxial films is not reported yet. The detailed and precise studies on rutile surfaces are supposed to offer valuable information in understanding and predicting anatase surfaces photochemistry,

which has been achieved. The surface structure of the rutile TiO_2(110) is the most extensively studied TiO_2 crystal facet. The structure is shown as Figure 6. Both

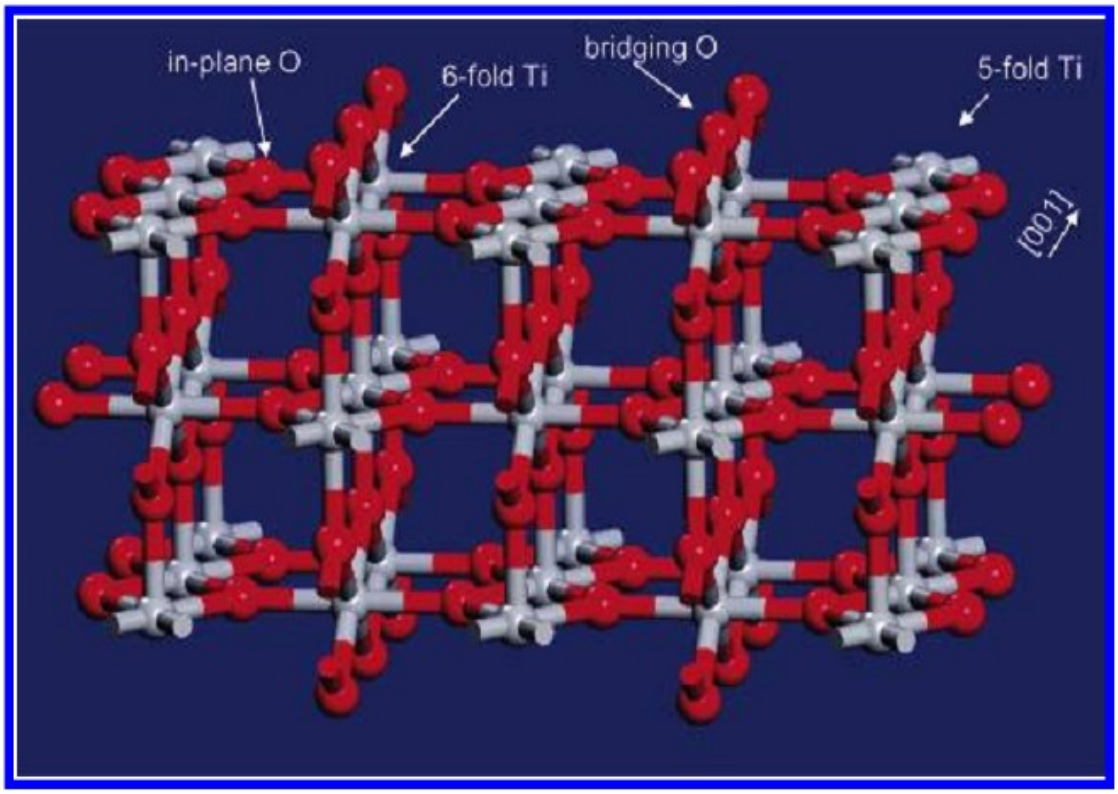

Figure 6. Surface structure of the stoichiometric TiO_2(110)-(1×1) surface depicting the two different types of surface titanium and oxygen atoms present. Reprinted with permission from ref 26. Copyright 2006 American Chemical Society

the 6-fold coordinated Ti atoms and 5-fold coordinated Ti atoms are in the same plane. The (110) surface contains rows of 2-fold coordinated oxygen atoms sitting directly on top of 6-fold coordinated Ti atoms. The rows of 5-fold and 6-fold Ti atoms are separated by rows of in-plane 3 fold-coordinated O atoms.

Both the theoretical method such as density of states (DOS) calculation[27] and experimental technique including surface X-ray diffraction (SXRD)[28] and low-energy electron diffraction (LEED)[29] have been employed to investigate the detailed structure information of the TiO_2(110) surface. The surface O atoms and Ti atoms are supposed to be located in distorted positions compared to the bulk counterparts. Recent LEED I/V show that an O atom outward relaxation of about 0.1 Å and an outward Ti atom relaxation of about 0.25 Å.[29]

1.3.2 Charge Carrier Excitation and Characterization

Electron-hole charge carriers pairs will be generated when the TiO_2 is irradiated by light with photons of energy higher than the band gap of TiO_2. To monitor the behavior of free charge carriers, electron paramagnetic resonance (EPR) spectroscopy and infrared (IR) spectroscopy are often used. It has been reported that under UV illumination, the photogenerated electrons are either trapped at localized states within the band gap and form a Ti^{3+}, which will be detected by EPR spectroscopy, or transit to the conduction band, which will be measured by IR spectroscopy.[30]

The Photogenerated holes also could be studied by using EPR as the holes will produce O^- species.[30]

EPR is broadly used to study the photogenerated charge carriers in metal oxides. Iyengar reviewed the use of EPR to study of UV-induced effects on TiO2 powders as

early as in 1972.[31] Grätzel studied the photogenerated electrons and holes at low temperature (4.2K) behavior in reduced anatase TiO_2 powder material.[32] Electrons are trapped by Ti^{4+} sites and produce Ti^{3+} in bulk, while holes are trapped at the surface and form as O^- species. A linear relationship between the numbers of photogenerated electrons and holes determined by EPR spectroscopy anatase TiO_2 is found.[30] At a high intensity UV irradiation, a deviation from linear correlation shows up, indicating that some of electrons transit to EPR-silent conduction band, which are IR-active and can be measured through IR spectroscopy.

In partially reduced TiO_2, the Ti^{3+} in the bulk of the material will give the same EPR signal as that of UV activated regular TiO_2 sample, and intensity is much higher than the latter. While the reduced TiO_2 shows no signal for O^-, which is quite different from the UV illuminated TiO_2.[30]

For semiconductors, excitation of electrons from the valence band to the conduction band can be achieved by various strategies, such as light irradiation, in which the photons energy is greater than the band gap of semiconductor. Payanotov etc. have reported a thermal excitation in vacuum for TiO_2-SiO_2 system.[33] They also observed the similar phenomenon in pure TiO_2 system.[34] This thermal excitation involves formation of shallow Ti^{3+} defect sites and electrons promotion from these defect sites to conduction band. The high density of states in conduction band make a continuum zone for electrons

transition, therefore will exhibit a continuous featureless background absorption in IR region. Yamakata et al. have studied the laser pulse excited Pt/TiO_2 sample with IR spectra and reported the observation of photoproduced conduction band electrons transition behaviors by IR excitation.[35] An interesting application associated with this phenomenon was reported by Baraton, who proved a sensor-like process for the electrons in TiO_2 conduction band.[36] When exposing the excited TiO_2 to oxidizing agents, the electrons in conduction band will be consumed and therefore a decrease in the IR absorption, while when treated with reducing agents, electrons from the reducing agents will be injected into the conduction band of TiO_2, then an enhancement of IR absorption can be observed.

1.3.3 Charge Transportation

The charge diffusion and mobility are associated with motion in a concentration gradient and an applied field, respectively. However, the charge transport (also called charge hopping) is a site-to-site transition.

a) Electron Transportation

The electrons transport in TiO_2 conduction band is one of the most important factors for photochemical process, as in which the electrons losing and/or gain are always involved. That explains why so many researches have been done on this issue. Van de Lagemaat and etc. have studied the electron transport in the anatase TiO_2 nanoporous film

for dye sensitized solar cell.[37] Many other forms of TiO_2, such as amorphous films,[38] nanoporous film of P25 (a mixture of anatase and rutile in the ratio of 3:1),[39] and rutile TiO_2 single crystals[40] have been selected as the research models for the transport of electrons. The theoretical and dynamic study of the transportation of electrons is also conducted by many groups too.[41-44]

So far, there is a lot of argument on how to model and explain the electron transport behavior in TiO_2.[45] It has been widely accepted that the transportation of electrons is quite different in nanoporous structures and single crystals.

For nanoporous networks, researchers initially thought that the electron trapping/detrapping process mainly control the electrons transport. De Jongh investigated the electrons transport in the P25 nanoporous film with modulated photocurrent spectroscopy and found that the transport was controlled by electron trapping/detrapping process on the surface states or at the particle boundaries.[46] Van de Frank studied electron transport in porous TiO_2 networks and also suggested a trapping and detrapping theory.[47] However, one year later, Frank and his coworkers overrode the conclusion they made and pointed out that the electron transport behavior did not match the trapping theory, as they failed to observe the photon flux dependence upon the activation energy (E_a).[37] It is expected that the E_a values will show a connection with the trap center distribution. In the case of deep traps, a low injection current is expected. However, this dependence was not

detected. Therefore, Frank proposed that structural disorder in porous network structure and interfaces between particles rather than the trap sites had a greater influence on electron transport. Turner measured the electron injection from dye R535 to P25 film by using a time-resolved terahertz spectroscopy and found the short distance of electron movement within the TiO_2 nanoparticles.[39] On the other hand, due to the disorder and boundaries within the film, the long distance electron transport is prohibited. Other groups also reported the similar results, i.e. the 'trapping/detrapping' theory was not a satisfactory model to depict the electron transport throughout the TiO_2. Boschloo et al. studied the electron movement in a ruthenium dye sensitized TiO_2 P25.[48] Interestingly, they observed that the electrons injected from dye to TiO_2 could be thermally excited with an E_a equal to 0.1-0.15 eV. They later suggested that the electron transport model should consider many factors, such as localized barriers between joint particles, electrostatics from high electron concentrations within particles and from the electron and counter cations at interfaces. Also, some researchers reported other factors to affect the electrons transport, for example, Agrell observed an electrolyte dragging effect on electrons movements,[49] and Eppler pointed out that some chemicals electron scavengers such as O_2 could enhance the electron transport.[50]

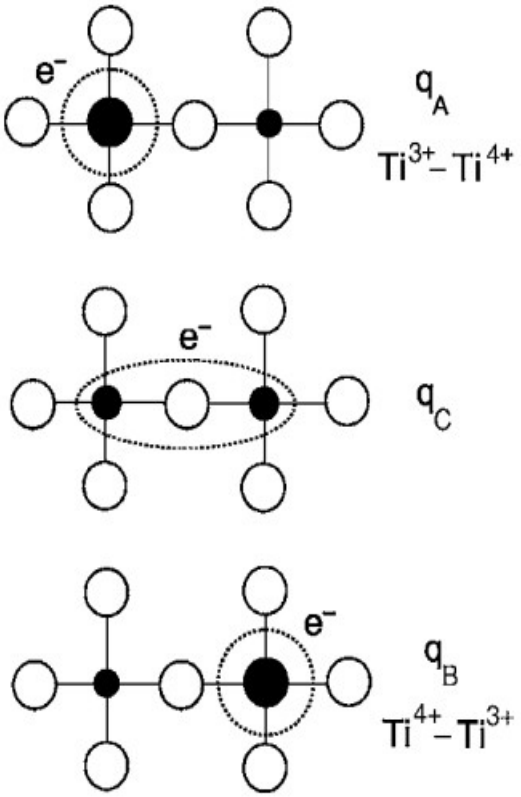

Figure 7. Schematic diagram of polaron e^- transfer. Designations 'q_A', 'q_B', and 'q_C ' correspond to the initial, final and transition state site configurations. Reprinted with permission from ref 52.

The electron transport in the single crystalline bulk TiO_2 is quite different from in the nanoparticles. In the anatase and rutile TiO_2 single crystals, there is a directional dependence for both electrons and holes transport. This anisotropic charge carrier movement has reported by many groups. Batista studied the electron transport in anatase TiO_2.[51] It was found that the injected electron from catechol showed an unevenly distribution throughout the single crystalline TiO_2. The time-dependent electron survival probabilities measurement confirmed that electron travelled fast along the surface

perpendicular <101> direction and the <010> direction, but slower along the <−101> directions. Note that the thermal fluctuations existing in the lattice could reduce much of the above anisotropy. Dupuis et al. measured the electrons and holes transport in bulk anatase and rutile TiO_2 based on Marcus theory for polaron hopping, as shown in Figure 7.[52] The hole hopping was found to be an adiabatic process with E_a values approximately twice that for electron hopping. Therefore one can expect that the lattice distortions around the holes play a much more important role to affect the holes transport than that of electrons. The E_a required for Electron and hole hopping to the rutile TiO_2(110) facets is expected to be higher than that in the bulk. One possible explanation is that the surface atoms will repel these charge carriers because of a lower dielectric constant for the surface compared to the bulk.

b) Hole Transportation

Compared to the electrons transportation, the researches on holes transportation are much less conducted. Unlike the electrons, the relationship between holes trapping and transport is still unclear. Though the holes transport is a key step in TiO_2 photocatalytic process, only a few experimental results from the studies of hole transport in TiO_2 have been reported. Duzhko proposed that electron transport diffusion coefficients in the TiO_2 conduction band are generally greater than those for holes in the valence band for both anatase and rutile phase.[53] However, Grela et al. observed that the holes moved to the

surface of TiO_2 nanoparticles (size < 5 nm) without complete thermalization, which indicated that the coupling between the holes and phonons may not be as efficient as the coupling between electrons and phonons.[54] Lantz and etc. utilized time-resolved second harmonic generation measurement to characterized the hole mobility in photoelectrodes composed by rutile single crystalline TiO_2.[55] The average time for holes diffusion from the bulk to the surface is 25 ps, and this value was found to be independent of applied bias or various electrolytes in the cell. Based on these experimental data, they calculated the average hole 'drift velocity' of ~ 4×10^4 cm/s, which is about one order of magnitude faster than the drift velocity of electrons reported other groups.[56]

1.3.4 Charge Carriers Trapping/Detrapping

Trapping and detrapping are significant steps for free charge carriers transfer in TiO_2, especially for TiO_2 photocatalytic process. The role the trapping plays is complicated, and could be either helpful or detrimental for photocatlytic reactions. If the trapping sites are located on the surface of photocatalyts, or if the trapping improves the electron-hole separation, then it should be treated as a positive effect. If the trapping centers are far from the electron/hole transfer sites, and result in fast recombination between electrons and holes, then trapping is detrimental for photocatalytic process. The trapping energy should be a suitable value, as too large will weaken the redox power of the electron/hole, and too small will be unable to play an important role for charge

separation. The trapping/detrapping rate is also a great concern for photocatalytic reactions.

1.3.4.1 Electron Trapping

Electron is usually reported to be trapped as localized Ti^{3+} sites in the TiO_2 lattice. Some factors, such as trapping energy, trapping site, kinetics, and concentration are needed fully consideration and understood.

a) Trapping Energy

Electrons will lose some energy after being trapped. The energy loss is estimated between 0.1 and 1 eV,[57] which agrees with the photoemission results from the surface of TiO_2 single crystal with electronic defects.[21] The energies of surface electron trap states are controlled by many aspects such as applied bias in an electrochemical condition, local atomic structure and dielectric properties, and the surface adsorbateds.[45] The trapping process probably could cause a structural relaxation and energy states localization. The distribution of trapping energies is believed to be an average of all existing different trap sites. So far, the origin of the trap sites distribution has not been fully understood, but is believed to be associated with the site heterogeneity.

b) Trapping Sites

To identify the trap sites, we need to understand which sites will achieve the most stabilization energy through localization of free electrons. However, so far, a lot of

debates existed in this area. Initially it thought that electrons would be preferentially trapped on the surfaces of TiO_2.[58] However, trapping electron in the bulk also was observed later.[59] Some group performed theoretical studies and claimed that bulk/subsurface trapping was prior to surface trapping.[60,61] Contrastly, theoretical calculation from some other groups indicated that the favorite electron trap sites were located in the under-coordinated Ti cations on the surfaces.[62] Some experimental data showed that the artificial process (such as heating) would produce the bulk electron trap.[63] Also, the electron traps were found at the grain boundaries and particle interfaces. Planelles et al. suggested that in the nanoporous TiO_2 structures, the pore size will greatly affect the electron trap stability, as the electronstatics at the pore walls are controlled by the pore size.[64] It was reported that when the pore size < 14 nm, the effect from the pore size will be observed. Szczepankiewicz et al. studied the FTIR spectra of TiO_2 and suggested that photogenerated electrons were preferentially trapped by surface OH groups.[65] They explained that the possible reason to make the Ti^{4+}-OH^- species a good electron traps was that the O-H stretching excitation energy matches the trapping energy well from the FTIR analysis.

Deskins employed the DFT+U calculations to study the rutile (110) facet.[66] Compared to the Ti underneath the bridging O, the subsurface Ti sites were energetically more favorable for electrons trapping. Their calculation showed that the surface five

coordinated Ti are good electron trapping sites and when going further into bulk (≥ 2 atomic layers), the Ti site are unfavorable for electrons trapping. Similar calculations for hydroxylated (110) surface, revealed that the introduction of OH group did not affect the preference for subsurface Ti sites and make the Ti sites below the OH group slight more favorable as surface traps.

By investigating the ultrafast spectroscopes of the excited TiO_2, researcher found that the electron trapping will occur very fast. Lots of groups suggested it only took as short as sub-picoseconds to trap an excited electron.[57]

While the electron trapping happening extremely fast, the lifetime of the trapped electrons is not necessary to be short, and actually, in some cases it could be as long as months. Rabani pointed out that electron trapping could be beneficial for electron/hole separation, as the electron trapping will compete with the electron/hole recombination even in the absence of hole scavengers.[67] Later, Peiró et al. confirmed this conclusion by examining the transient absorption spectra of TiO2 films.[68] They found that without the holes scavenger ethanol and electrons scavenger O_2, the transient signal at 800 nm attributed to excitation of trapped electrons showed a long half-life of ~25 μs, indicating a slow electron/hole recombination at trap sites. And in the presence of hole scavenger such as ethanol, the life time of the trapped electrons will be elongated to ~0.5 s.

c) Trapped Electron Characterization

Electron paramagnetic resonance (EPR) is an extensive technique used by many to characterize trapped electrons in TiO_2.[45] The difference in spin state

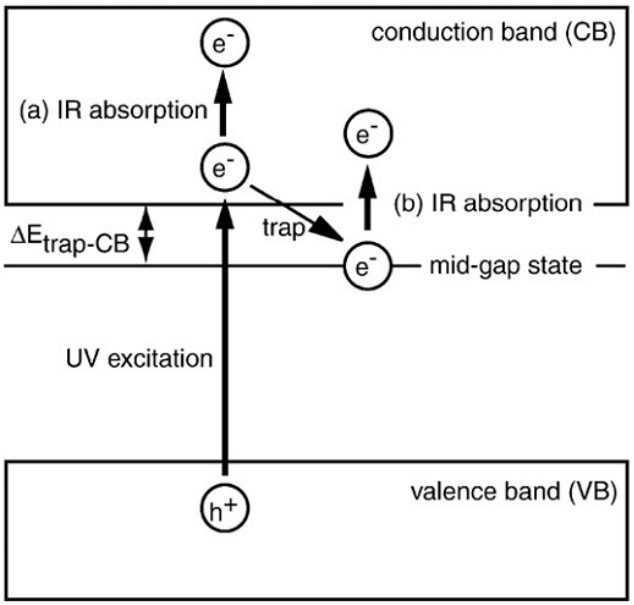

Figure 8. Schematic illustration of possible optical transitions associated with excited electrons following band-to-band transitions in TiO_2. (a) CB electrons and (b) trapped electrons. Reprinted with permission from ref 58. Copy right 2005, with permission from Elsevier.

environments between trapped electrons (usually detected as Ti^{3+}) and trapped holes (usually detected as O^-) could be easily distinguished by EPR. Other techniques, such as optical spectra also have been utilized to detect the trapped electrons in TiO_2. Figure 8 gives a schematic picture to show the light excitation events in TiO_2. The near UV light will promote the electrons from to conduction band. While for the trapped electrons, the IR will be energy-sufficient to excite them from localized Ti^{3+} into conduction band.

d) Electron Detrapping

Detrapping of electrons could be considered to two different type: polaronic hopping, which could be thought as 'trap-to-trap' hopping, and real detrapping, in which case the localized trapped electrons are promoted into conduction band and become real free electrons. Two common methods to achieve the detrapping electrons are thermal activation and non-thermal activation such as sub-bandgap light excitation.

Van de Lagemaat pointed out that thermal detrapping on TiO_2 occurred at a rate as fast as 10^8 events per second based on their sensitization studies at room temperature.[37] The non-thermal optical detrapping is controlled by the optical characters of the trap state. Shkrob et al. reported that either 532 nm or 1064 nm light could induce the electron detrapping in colloidal anatase TiO_2.[69] Komaguchi and etc. investigated the Ti^{3+} EPR signals in thermally reduced anatase, rutile and mixture P25 during and after visible light irradiation.[70,71] For reduced anatase and rutile, the ESR signals showed an obvious decrease during visible light irradiation, which was accounted to detrapping of electrons from the localized Ti^{3+} to free delocalized conduction band electrons. After the light was removed, the ESR signals restored for both anatase and rutile. However, in the case of P25, the EPR signal increased when shined by visible light. They proposed that when activated b, the electron detrapped from the anatase component in the P25, but retrapped by the rutile, giving a stronger signal than anatase at the same spin density.

1.3.4.2 Hole Trapping

Compared to the electrons trapping, the studied on hole trapping are more difficult to control and characterize. A dye sensitization and electron injection could provide a good research model for electrons trapping, but for hole, it is hard to achieve a facile method to inject holes into the TiO_2 valence band. Therefore, most of investigation focused on the band-to-band excitation process, since it is crucial for understanding TiO_2 photocatalytic chemistry.

Some group studied the EPR spectra and suggested that the most favorite trapping sites for holes are located at surface Ti^{4+}–O^{-} site, where the hole stays at an under-coordinated oxygen atom.[59,72] However, it is still unclear which is the preferred trapping site between bridged oxygen and oxo oxygen. Thurnauer studied hole trapping on the surfaces of P25 and rutile through EPR measurements.[73] They found that after replacing the H in surface -OH groups with D, the O^{-} line shape kept unchanged. In contrast, after introduction of surface O^{17}, the oxygen EPR line shape changed. So they proposed that holes would not be trapped by surface protonated oxygen anion sites. Kerisit et al. studied the holes trapping at the unrelaxed rutile(110) facet by electrostatic calculations.[74] They found that holes preferred being trapped in the near-surface region, and for comparing, electrons favored subsurface sites.

Similar to the electron trapping, the hole trapped also could be tracked by EPR and optical spectra. However, the precise assignment of the signals in the spectra to specific holes excitation is still a big chanllenge.[45]

Thomson and Yates pointed out that the stability of holes in TiO_2 is different between surface trapped holes and the near-sruface trapped hole. In s system with neither electrons scavengers nor holes scavengers, the surface trapped holes could be survive up to ~ 180 K, above which, the hole will be annihilated by electrons.[59] When an electron scavenger is present, the lifetimes of the trapped holes are in the range of milliseconds to minutes.[75]

Hole trapping on the surfaces of TiO_2 could occurred as rapidly as electron trapping. Yang and Tamai pointed out that the timescale of a hole trapping at the surface of anatase nanoparticles is of ~ 50 fs.[76] It was found that the holes trapping was unable to compete with electron injected from hole scavengers well such as SCN^- and CH_3OH. Interestingly, Shen et al. reported that the lifetimes of trapped holes in rutile were longer than that in anatase.[77] Deskins predict the same conclusion according to his theoretical calculation.[78]

1.3.5 Charge Carriers Recombination

Similar to all the other semiconductors, the electron-hole recombination is a common reason detrimental to photocatalytic activity of TiO_2. The recombination can be

classified into two types: radiative recombination and non-radiative recombination. Usually, the non-radiative recombination is more favorable than the radiative recombination. However, the ratio between the two recombination types could be tunable by many strategies such as introduction of dopants or heterojuctions.

1.3.5.1 Radiative Recombination

Radiative decay, also called photoluminescence, is usually at sub-band gap energies owing to carrier relaxation and trapping. Therefore, photoluminescence spectrum is a good media for researchers to investigate the dynamics and structural properties of TiO_2. Character photoluminescence peak in anatase phase TiO_2 is located at ~540 nm due to the decay of self-trapped excitons. It has been reported that the surface condition and the nanosize of anatase greatly influence the photoluminescence spectra. Compared to rutile TiO_2, the anatase TiO_2 possesses a heavier distortion TiO_6 octahedral structure, which may result in the exciton binding.[79] In addition, the lattice density of anatase is slightly lower than that of rutile (3.89 g/cm3 *vs* 4.25 g/cm3), which make the distortion more readily occur in anatase than in rutile. Self-trapped exciton photoluminescence shows the anisotropism, i.e. strong emission component in normal directions of the c-axis while weak component in the parallel directions to the c-axis.[80] The lifetime of photoluminescence in anatase is typically on nanoseconds scale. Murakami studied the photoluminescence decay profile of the anatase (001) film

epitaxial growth on (100) LaAlO3, and pointed out that recombination at higher temperature (>200K) will prefer the non-radiative owing to the more active lattice motions.[80] Tang et al. suggested that bulk defects and dopants in anatase will affect self-trapped luminescence state.[81] Zhu reported after introducing the –OH and $–OCH_2CH_3$ groups to the surface of 4 nm anatase nanoparticles, a new photoluminescence show up at ~474 nm.[82] Yoon observed three luminescence peaks at 420 nm, 470 nm and 550 nm in a liposome modified anatase nanoparticles.[83] Researches also indicated that interfaces between the anatase and the substrates play an important role in photoluminescence.

For rutile TiO_2, researchers suggested that the defects, surface atoms, and impurities induce the photoluminescence. Nakamura reported that photoluminescence could be observed from the single crystal rutile (110) and (100) facets.[84] However, after photo etching the surface in $HClO_4$, the photoluminescence was gone. They ran a series of controlled experiments and found the only the smooth surface will be active for photoluminescence, and the rough surface was not, which may imply that well ordered surface is indispensible to produce photoluminescence in rutile TiO_2. This may also explain why there was no photoluminescence for amorphous TiO_2 although the recombination is common on the surface.

1.3.5.2 Non-Radiative Recombination

Many researches have confirmed that the non-radiative recombination is dominating in nature for TiO_2.[57] As we discussed before, the crystallinity of TiO_2 significantly influence the recombination process.

Shockley has pointed out that non-radiative charge carriers recombination behavior can be explained by a Shockley-Read-Hall model.[85] This theory describes the possible process for capture of free charge carriers electrons and/or holes at trap sites in the bulk. As long as the free charge carriers are trapped by the recombination centers, they will be annihilated by their counterpart (holes or electrons). Various sites, including crystalline defects (such as interstitial atoms), grain boundaries and etc. can work as recombination centers. In the Shockley-Read-Hall theory, it is proposed a four–step process for lectron-hole recombination. 1) electron capture. The free electrons drop from the conduction band and are trapped by electron capture sites. 2) electrons emission. Not all the trapped electron will be annihilated and some of trapped electrons have the chance to reemitted into conduction band and become free charge carriers. 3) hole capture. For the electrons trapped in the trapping sites, they readily transit into valence band and are captured by holes, ending with the recombination. 4) hole emission. Like electrons, the electrons in the valence band also could be promoted into the trapping sites. According to the Shockley-Read-Hall theory, the number of recombination centers is very low

compared to the total number of all the charge carriers. Thompson reported that in the case of rutile TiO_2(110) facet, the density of hole-trapping sites was estimated to be the order of 2.5×18 cm^{-3}, only taking up a portion of 3×10^{-5} of the bulk atoms of TiO2 crystal.[86]

The non-radiative recombination is not easy to direct measure, so researchers usually study it by catching the heat released from non-radiative recombination. So far, the systematic studies on the correlations between recombination rates and the free charge carriers concentration or locations are still rare. Rabani pointed out that the high charge density will enhance the recombination and electron scavengers will help depress the recombination.[67] The surface trapping/detrapping process, the surface area, phase composition, particle size, and etc are connected to the recombination rates.

Many debates are present about the recombination kinetics. Some researcher suggested a second order decay kinetics.[87] However, others claimed that the recombination is first order, and will become second order with rate asymptotically approaching a $t^{-1/2}$ dependence due to the exciton–exciton proximity.[88] If electrons or holes are tightly trapped and the counterparts are free, the kinetics could not follow the second oder. Tamaki et al. even proposed a multiexponential decay kinetics as they thought that the diffusion rates would greatly affect the recombinations.[89]

1.4 Synthesis of TiO_2

As one of the most promising photocatalysts, TiO_2 has attracted massive research interests. Prior to understanding the structure-property relationship, morphology-property relationship, and further improving its photocatalytic activity, the very first issue need to be addressed is how to synthesize TiO_2 materials in various phase compositions, different shapes, and desired sizes from a facile, economic and controllable method. So far, lots of synthetic strategies have been introduced and developed well.[90]

1.4.1 Sol-Gel Method

The sol gel method is originally and widely used in ceramic materials preparation. A sol gel process includes two typical steps: 1) Precursors, usually metal salts, are hydrolyzed and form a sol colloidal suspension. 2) The liquid sol polymerizes, loses solvent and converts to solid gel. The gel then could be used as a good starting material to process and made TiO_2 in different morphologies. For example, by a simple dip coating or spin coating technique, TiO_2 film can be fabricated on various substrates. Porous aerolel could be formed after removing the solvent from the gel under a supercritical condition. A representative method to synthesize the TiO_2 nanomaterials is the hydrolysis of a titanium alkoxide through an acid catalyzed process followed by condensation. In the case of low amount of water, low hydrolysis rates, and excess titanium alkoxide, a three dimensional polymeric Ti-O-Ti skeletons with close packing will be formed. Closed

packed TiO_2 particles can be prepared later from this three dimensional skeleton. In a condition of medium amount of water and high hydrolysis rate, $Ti(OH)_4$ will be produced. In this case, the large amount of Ti-OH group make the it difficult to develop a three dimensional skeletons and so only loosely packed particles would be formed. Oskam et al. investigated the growth kinetics of TiO_2 nanoparticles in titanium tetraisopropoxide (TTIP), and pointed out that the coarsening rate constant increased with temperature, as the viscosity of the precursor solution and TiO_2 solubility were greatly affected by the temperature.[91] They also observed that the secondary particles will be formed through the self-assembly of primary nanoparticles under high temperature for a long reaction time. Also, as expected, the average diameter of the nanoparticles shows a linear correlation with the reaction time.

A typical procedure to produce high quality crystalline anatase TiO_2 nanoparticles with controllable sizes and morphologies is the condensation of titanium alkoxide in the assistance of surfactants such as tetramethylammonium hydroxide. Sugimoto studied the how the experimental parameters, such as pH values, reaction temperature, time, surfactants and etc. will influence the sizes and shapes of the TiO_2 nanomaterials[92-96]. The morphology control is achieved by governing the growth rate of different crystal facets of TiO_2 nuclei through selective adsorption of surfactants to desired planes.

In addition of the surfactant soft template method, the shape control was also achieved by using hard template. Anodic alumina membrane (AAM) is a widely used template for nanomaterials preparation. Miao et al. synthesized TiO_2 nanorods by dipping porous AAMs into a boiled TiO2 sol followed by drying and heating processes.[97] Anatase nanorods and rutile nanorods could be formed under low calcinations temperature and high calcinations temperature, respectively. The size of the nanorods can be tuned by using AAM templates with different pore sizes. Lin reported prepared ordered TiO_2 nanowire arrays through electrophoretic deposition of TiO_2 titanium isopropoxide (TTIP) suspensions into AAM.[98] He pointed out that in order to synthesize nanowires rather than nanorods, the AAM should have long pores. By treatment of the AAM soaked in TiO_2 sol in vacuum, and then removing the AAM, the TiO_2 nanotubes will be fabricated.[99] In this vacuum treatment, the entire volume of the solution in the pore of the AAM was pulled out. Therefore the final products are nanotubes instead of nanorods. Also, Qiu et al. used the ZnO nanorods array as the template and successfully prepared TiO_2 nanotube on the glass substrates.[100]

1.4.2 Hydrothermal Method

Hydrothermal synthesis is versatile and extensively used in nanomaterials synthesis. The reagents are usually placed into a Teflon liner and then enclosed by a steel autoclave. The temperature could be up to 220 °C, as beyond which the Teflon liner will

be destroyed. If the Teflon liner is removed from the reaction system and the reagent directly placed into a sealed steel high pressure vessel, then the hydrothermal reaction temperature could be as high as 500 °C. In the internal of the autoclave, the high vapor pressure and high temperature of aqueous solution could induce some reactions which cannot occur under regular conditions. Yang et al. synthesized TiO_2 nanoparticles by hydrothermal treatment of precipitates from tetraalkylammonium hydroxides peptized titanium butoxide aqueous solution.[101] They found that the size of the particles size decreased as longer alkyl chain in titanium precursors. Chae also reported hydrothermal treatment of TTIP acidic ethanol aqueous solution to prepare TiO_2 nanoparticles.[102] The particle size was tunable in the range of 7-25 nm as changing the concentration of Ti precursor and the composition of the ethanol/H_2O solvent. The TiO_2 nanorodes were prepared by hydrothermal reaction from a dilute $TiCl_4$ solution.[103] TiO_2 nanorod array was also fabricated on the glass substrate by hydrothermal treatment of $TiCl_3$ salt solution.[104]

A typical method to prepare TiO_2 nanowires is to hydrothermally treat the TiO_2 powders in a high concentrated NaOH (15 M for example) solution.[105] TiO_2 nanowires also could be made from exfoliation of layered titanate precursors.[106] Wei et .al reported that by exfoliating $Na_2Ti_3O_7$ with dilute HCl, the TiO_2 nanosheets were formed, and then the nanosheets would self-split into nanowires to relase the surface stress.

A facile and widely used strategy to fabricate TiO_2 nanotubes was developed by Kasuga.[107] Similar to the above mentioned concentrated NaOH hydrothermal treatment of TiO_2 powder to prepare TiO_2 nanowires, they used more concentrated NaOH solution (20 M), and ran the hydrothermal reaction at a lower temperature (110 °C vs 200 °C), then rinse the products with dilute HCl solution, and then the nanotubes were prepared. They proposed the formation of TiO_2 nanotubes included the following steps: 1) The concentrated NaOH aqueous will break some of Ti-O-Ti bonds in the raw TiO_2 particles, and made some Ti-O-Na and Ti-O-H bonds. The Ti-OH bond could form a sheet 2) After the products washed by dilute HCl solution and distilled water, the dehydration of Ti-OH bonds by HCl occurred, and new Ti-O-Ti bonds or Ti-O-H-O-Ti hydrogen bonds were produced. 3) Since the bond distance from one Ti to the next Ti on the surface decreased, the sheet would fold and connect the both ends and form a tube structure. According to this mechanism, the TiO_2 nanotubes were formed after the HCl treatment. However, Du pointed out that the nanotubes were formed when the concentrated NaOH solution treating the TiO_2 powders.[108] A new 3D-2D-1D mechanism was proposed by Wang et al.[109] They suggested that after treated by NaOH, the Ti-O-Ti bonds partially broke and form a zigzag structure through edges share between the free TiO_6 octahedrons along [100] direction. Later, what will happen is the two-dimensional sheets were formed by the oxo bridges between the Ti centers in the [001] direction. Finally, two-dimensional

sheets rolled up to saturate the dangling bonds on the ends, producing the TiO_2 nanotubes.

1.4.3 Solvothermal Method

The solvothermal method is developed from the hydrothermal method. The only different in the methodology is the solvothermal method uses the organic solvent to replace the water in hydrothermal method. This small change in methodology actually results in a huge difference in the following reactions. First of all, the higher liquid temperature could be achieved as the boiling point of some organic solvent can be much higher than that of water. Also, more viscosity tuning from various choice of organic solvents can provide a better manage on the growth rate of nanomaterials. Like the hydrothermal method, the solvothermal method is versatile and usually shows a more precise control upon the size distribution and dispersity.

Nanoparticles and nanorods with high quality and narrow size distrubition have reported through solvothermal method.[110] Interestingly, similar to hydrothermal treatment TiO_2 powder in concentrated NaOH solution, the same strategy could be used in solvothermal method to prepare nanowires.[111] The solvent here played a significant role to control the morphology of the TiO_2 products. It was suggested that solvents with different physical and chemical properties can greatly affect the solubility, reactivity, and diffusion behavior of the TiO_2 reagents, and so the morphology and the crystallization

behavior of the final products. The organic solvent, such as ethanol, will affect the polarity of the reactant particles and the viscosity of the solution. Therefore, they found that in case of no ethanol, only short and wide flake-like structures, instead of nanowires TiO_2 would be produced. When the author using other organic solvent, such as chloroform to replace the ethanol, TiO_2 nanorods were obtained.[112]

1.4.4 Chemical and Physical Vapor Method

Vapor deposition means a process in which vapor materials are condensed to solid materials. The technique was originally developed to coat various substrates so as to modify the substrates' mechanical, electrical, thermal, optical, corrosion resistance, and wear resistance properties. Now it has been widely used in semiconductor industry to produce high-purity and high-quality thin film. In a typical process, the substrates are placed into a vacuum chamber and condense the target products. If chemical reactions occur during the process, it is called chemical vapor deposition (CVD); if no chemical reactions involved, it is call physical vapor deposition (PVD). Seifried et al. reported that thick titania films, consisting of nanocrystalline grains smaller than 25 nm, can be made by pyrolysis of TTIP in a helium/oxygen mixed atmosphere.[113] Pradhan et al. successfully fabricated TiO_2 nanorod arrays with a diameter below 100 nm and a length of 0.5-2 μm on WC-Co substrates by metal organic CVD (MOCVD) with TTIP as the precursor.[114]

Some strategies derived from the classic CVD methods also have been used to synthesize various TiO_2 nanomaterials, such as electrostatic spray hydrolysis,[115] diffusion flame pyrolysis,[116] thermal plasma pyrolysis,[117] and etc.

Unlike CVD which involves chemical reaction in evaporation and deposition process, in PVD process the products materials are directed evaporated and then condensed into solids on substrates. PVD methods include many different techniques, such as ion plating and implantation, sputtering, laser vaporization, and etc. TiO_2 nanowire arrays have been prepared through a facile PVD approach by many groups.[118]

1.4.5 Anodic Oxidizing Method

Grimes invented a very sample but very effective method, i.e. anodic oxidation of Ti foil approach, to prepared TiO_2 nanotube arrays.[119] In a typical experiment run, a two-electrode reaction cell is set up, with Ti foil as anode and platinum as cathode. A deionized and acetone treated Ti foil was place into a 0.5% HF aqueous solution and undergo a anodic oxidization under 10-20 V for 10-30 min. Then the anodized Ti foil was annealed in oxygen atmosphere at 500 °C for 6h, and crystallized TiO_2 nanotubes were formed on Ti substrate. They extensively study the effects of experimental parameters, and found that the diameter and length TiO_2 nanotubes could be tuned in a broad range (15-120 for diameter and 20 nm to 10 μm for length) by adjusting the applied potential from 1 V to 25 V and the composition of phosphate/HF electrolytes.[120]

1.5 Contributions from Our Work[121-123]

In Chapter 2, we investigated the Ti^{3+}-doped TiO_2 by a facile one-step combustion method. It is found that Ti^{3+} extends the photoresponse of TiO_2 from the UV to the visible light region, which leads to high visible-light photocatalytic activity for the generation of hydrogen gas from water. It worth note that unlike some traditional method, such as vacuum anneal, H_2 reduction or UV light irradiation, the Ti^{3+} was exclusively found in the bulk of the as-prepared sample through the combustion method, which grant a very good stability to our sample.

We further studied how the synthetic conditions such as crystallinity, surface area, particle size, crystal facets distribution and etc. affected the photocatalytic activity of the partially reduced TiO_2, in order to understand the chemistry behind the reaction, and to optimize the synthetic parameters. This part will be covered in Chapter 2.

In addition, we found that the partially reduced TiO_2 with highly active facets could be fabricated by a facile hydrothermal treatment of the Ti powder and hydrochloric acid. We offered a simple surfactant-free method to prepare Ti^{3+} doped TiO_2 singe crystals with highly active facets developed preferentially, which is supported by the electron paramagnetic resonance (EPR) spectra and transmission electron microscopy (TEM), respectively. The as-synthesized single crystal sample shows a great improvement in the photocatalytic H_2 production activity over our previously prepared

particles. It is inferred that the active facets play a crucial role for this enhancement. Measurement of the photocatalytic activity over an extended time period proved the excellent stability of the reduced TiO_2 made by this approach.

1.6 References

(1) "U.S. EIA International Energy Statistics". Retrieved 2010-01-12.

(2) Lewis, N. S.; Nocera, D. G. *Proc. Natl. Acad. Sci. U. S. A.* **2006**, *103*, 15729-15735.

(3) Fujishima, A.; Honda, K. *Nature* **1972**, *238*, 37-38.

(4) Osterloh, F. E. *Chem Mater* **2008**, *20*, 35-54.

(5) Alexander, B. D.; Kulesza, P. J.; Rutkowska, L.; Solarska, R.; Augustynski, J. *J Mater Chem* **2008**, *18*, 2298-2303.

(6) Reber, J. F.; Meier, K. *J Phys Chem-Us* **1984**, *88*, 5903-5913.

(7) Spathis, P.; Poulios, I. *Corros Sci* **1995**, *37*, 673-680.

(8) Sato, S.; White, J. M. *Chem Phys Lett* **1980**, *72*, 83-86.

(9) Yamaguti, K.; Sato, S. *J Chem Soc Farad T 1* **1985**, *81*, 1237-1246.

(10) Kato, H.; Asakura, K.; Kudo, A. *J Am Chem Soc* **2003**, *125*, 3082-3089.

(11) Inoue, Y.; Niiyama, T.; Asai, Y.; Sato, K. *J Chem Soc Chem Comm* **1992**, 579-580.

(12) Maeda, K.; Teramura, K.; Lu, D. L.; Takata, T.; Saito, N.; Inoue, Y.; Domen, K. *Nature* **2006**, *440*, 295-295.

(13) Sayama, K.; Mukasa, K.; Abe, R.; Abe, Y.; Arakawa, H. *Chem Commun* **2001**, 2416-2417.

(14) Hitoki, G.; Takata, T.; Kondo, J. N.; Hara, M.; Kobayashi, H.; Domen, K. *Chem Commun* **2002**, 1698-1699.

(15) Kim, H. G.; Hwang, D. W.; Kim, J.; Kim, Y. G.; Lee, J. S. *Chem Commun* **1999**, 1077-1078.

(16) Kim, H. G.; Becker, O. S.; Jang, J. S.; Ji, S. M.; Borse, P. H.; Lee, J. S. *J Solid*

State Chem **2006**, *179*, 1214-1218.

(17) Kudo, A.; Kato, H. *Chem Lett* **1997**, 421-422.

(18) Zou, Z. G.; Arakawa, H. *J Photoch Photobio A* **2003**, *158*, 145-162.

(19) Kudo, A.; Miseki, Y. *Chem Soc Rev* **2009**, *38*, 253-278.

(20) Rajeshwar, K.; de Tacconi, N. R.; Chenthamarakshan, C. R. *Chem Mater* **2001**, *13*, 2765-2782.

(21) Diebold, U. *Surf Sci Rep* **2003**, *48*, 53-229.

(22) Bakardjieva, S.; Stengl, V.; Szatmary, L.; Subrt, J.; Lukac, J.; Murafa, N.; Niznansky, D.; Cizek, K.; Jirkovsky, J.; Petrova, N. *J Mater Chem* **2006**, *16*, 1709-1716.

(23) Di Paola, A.; Addamo, M.; Bellardita, M.; Cazzanelli, E.; Palmisano, L. *Thin Solid Films* **2007**, *515*, 3527-3529.

(24) Hall, S. R.; Swinerd, V. M.; Newby, F. N.; Collins, A. M.; Mann, S. *Chem Mater* **2006**, *18*, 598-600.

(25) Addamo, M.; Bellardita, M.; Di Paola, A.; Palmisano, L. *Chem Commun* **2006**, 4943-4945.

(26) Thompson, T. L.; Yates, J. T. *Chem Rev* **2006**, *106*, 4428-4453.

(27) Swamy, V.; Muscat, J.; Gale, J. D.; Harrison, N. M. *Surf. Sci.* **2002**, *504*, 115-124.

(28) Charlton, G.; Howes, P. B.; Nicklin, C. L.; Steadman, P.; Taylor, J. S. G.; Muryn, C. A.; Harte, S. P.; Mercer, J.; McGrath, R.; Norman, D.; Turner, T. S.; Thornton, G. *Phys Rev Lett* **1997**, *78*, 495-498.

(29) Lindsay, R.; Wander, A.; Ernst, A.; Montanari, B.; Thornton, G.; Harrison, N. M. *Phys Rev Lett* **2005**, *94*.

(30) Berger, T.; Sterrer, M.; Diwald, O.; Knozinger, E.; Panayotov, D.; Thompson, T. L.; Yates, J. T. *J Phys Chem B* **2005**, *109*, 6061-6068.

(31) Iyengar, R. D.; Codell, M. *Adv Colloid Interfac* **1972**, *3*, 365-388.

(32) Howe, R. F.; Gratzel, M. *J Phys Chem-Us* **1987**, *91*, 3906-3909.

(33) Panayotov, D.; Yates, J. T. *Chem Phys Lett* **2003**, *381*, 154-162.

(34) Panayotov, D. A.; Yates, J. T. *Chem Phys Lett* **2005**, *410*, 11-17.

(35) Yamakata, A.; Ishibashi, T.; Onishi, H. *Chem Phys Lett* **2001**, *333*, 271-277.

(36) Baraton, M. I.; Merhari, L. *Nanostruct Mater* **1998**, *10*, 699-713.

(37) van de Lagemaat, J.; Frank, A. J. *J Phys Chem B* **2001**, *105*, 11194-11205.

(38) Solbrand, A.; Henningsson, A.; Sodergren, S.; Lindstrom, H.; Hagfeldt, A.; Lindquist, S. E. *J Phys Chem B* **1999**, *103*, 1078-1083.

(39) Turner, G. M.; Beard, M. C.; Schmuttenmaer, C. A. *J Phys Chem B* **2002**, *106*, 11716-11719.

(40) Itoh, C.; Iwahashi, K.; Kan'no, K. *Nucl Instrum Meth B* **2002**, *191*, 271-274.

(41) Usami, A. *Chem Phys Lett* **1998**, *292*, 223-228.

(42) Mora-Sero, I.; Anta, J. A.; Dittrich, T.; Garcia-Belmonte, G.; Bisquert, J. *J Photoch Photobio A* **2006**, *182*, 280-287.

(43) Usami, A.; Ozaki, H. *J Phys Chem B* **2001**, *105*, 4577-4583.

(44) Cass, M. J.; Qiu, F. L.; Walker, A. B.; Fisher, A. C.; Peter, L. M. *J Phys Chem B* **2003**, *107*, 113-119.

(45) Henderson, M. A. *Surf Sci Rep* **2011**, *66*, 185-297.

(46) de Jongh, P. E.; Vanmaekelbergh, D. *Phys Rev Lett* **1996**, *77*, 3427-3430.

(47) van de Lagemaat, J.; Frank, A. J. *J Phys Chem B* **2000**, *104*, 4292-4294.

(48) Boschloo, G.; Hagfeldt, A. *J Phys Chem B* **2005**, *109*, 12093-12098.

(49) Agrell, H. G.; Boschloo, G.; Hagfeldt, A. *J Phys Chem B* **2004**, *108*, 12388-12396.

(50) Eppler, A. A.; Ballard, I. N.; Nelson, J. *Physica E* **2002**, *14*, 197-202.

(51) Rego, L. G. C.; Batista, V. S. *J Am Chem Soc* **2003**, *125*, 7989-7997.

(52) Deskins, N. A.; Dupuis, M. *Phys Rev B* **2007**, *75*, 195212

(53) Duzhko, V.; Timoshenko, V. Y.; Koch, F.; Dittrich, T. *Phys Rev B* **2001**, *64*.

(54) Grela, M. A.; Brusa, M. A.; Colussi, A. J. *J Phys Chem B* **1997**, *101*, 10986-10989.

(55) Lantz, J. M.; Corn, R. M. *J Phys Chem-Us* **1994**, *98*, 9387-9390.

(56) Salafsky, J. S. *Phys Rev B* **1999**, *59*, 10885-10894.

(57) Leytner, S.; Hupp, J. T. *Chem Phys Lett* **2000**, *330*, 231-236.

(58) Yamakata, A.; Ishibashi, T.; Onishi, H. *J Mol Catal a-Chem* **2003**, *199*, 85-94.

(59) Ke, S. C.; Wang, T. C.; Wong, M. S.; Gopal, N. O. *J Phys Chem B* **2006**, *110*, 11628-11634.

(60) Shapovalov, V.; Stefanovich, E. V.; Truong, T. N. *Surf. Sci.* **2002**, *498*, L103-L108.

(61) Kowalski, P. M.; Camellone, M. F.; Nair, N. N.; Meyer, B.; Marx, D. *Phys Rev Lett* **2010**, *105*.

(62) Qu, Z. W.; Kroes, G. J. *J Phys Chem B* **2006**, *110*, 8998-9007.

(63) Nakaoka, Y.; Nosaka, Y. *J Photoch Photobio A* **1997**, *110*, 299-305.

(64) Planelles, J.; Movilla, J. L. *Phys Rev B* **2006**, *73*, 235350.

(65) Szczepankiewicz, S. H.; Moss, J. A.; Hoffmann, M. R. *J Phys Chem B* **2002**, *106*, 2922-2927.

(66) Deskins, N. A.; Rousseau, R.; Dupuis, M. *J Phys Chem C* **2009**, *113*, 14583-14586.

(67) Rabani, J.; Yamashita, K.; Ushida, K.; Stark, J.; Kira, A. *J Phys Chem B* **1998**, *102*, 1689-1695.

(68) Peiro, A. M.; Colombo, C.; Doyle, G.; Nelson, J.; Mills, A.; Durrant, J. R. *J Phys Chem B* **2006**, *110*, 23255-23263.

(69) Shkrob, I. A.; Sauer, M. C. *J Phys Chem B* **2004**, *108*, 12497-12511.

(70) Komaguchi, K.; Nakano, H.; Araki, A.; Harima, Y. *Chem Phys Lett* **2006**, *428*, 338-342.

(71) Komaguchi, K.; Maruoka, T.; Nakano, H.; Imae, I.; Ooyama, Y.; Harima, Y. *J Phys Chem C* **2010**, *114*, 1240-1245.

(72) Hurum, D. C.; Gray, K. A.; Rajh, T.; Thurnauer, M. C. *J Phys Chem B* **2005**, *109*, 977-980.

(73) Dubinski, A. A.; Perekhodtsev, G. D.; Poluektov, O. G.; Rajh, T.; Thurnauer, M. C. *J Phys Chem B* **2002**, *106*, 938-944.

(74) Kerisit, S.; Deskins, N. A.; Rosso, K. M.; Dupuis, M. *J Phys Chem C* **2008**, *112*, 7678-7688.

(75) Grela, M. A.; Colussi, A. J. *J Phys Chem B* **1999**, *103*, 2614-2619.

(76) Yang, X. J.; Tamai, N. *Phys Chem Chem Phys* **2001**, *3*, 3393-3398.

(77) Shen, Q.; Katayama, K.; Sawada, T.; Yamaguchi, M.; Kumagai, Y.; Toyoda, T. *Chem Phys Lett* **2006**, *419*, 464-468.

(78) Deskins, N. A.; Dupuis, M. *J Phys Chem C* **2009**, *113*, 346-358.

(79) Tang, H.; Berger, H.; Schmid, P. E.; Levy, F. *Solid State Commun* **1994**, *92*,

267-271.

(80) Murakami, M.; Matsumoto, Y.; Nakajima, K.; Makino, T.; Segawa, Y.; Chikyow, T.; Ahmet, P.; Kawasaki, M.; Koinuma, H. *Appl. Phys. Lett.* **2001**, *78*, 2664-2666.

(81) Tang, H.; Berger, H.; Schmid, P. E.; Levy, F.; Burri, G. *Solid State Commun* **1993**, *87*, 847-850.

(82) Zhu, Y. C.; Ding, C. X.; Ma, G. H.; Du, Z. L. *J Solid State Chem* **1998**, *139*, 124-127.

(83) Yoon, M.; Seo, M.; Jeong, C.; Jang, J. H.; Jeon, K. S. *Chem Mater* **2005**, *17*, 6069-6079.

(84) Nakamura, R.; Okamura, T.; Ohashi, N.; Imanishi, A.; Nakato, Y. *J Am Chem Soc* **2005**, *127*, 12975-12983.

(85) Shockley, W.; Read, W. T. *Phys Rev* **1952**, *87*, 835-842.

(86) Thompson, T. L.; Yates, J. T. *J Phys Chem B* **2005**, *109*, 18230-18236.

(87) Colombo, D. P.; Bowman, R. M. *J Phys Chem-Us* **1996**, *100*, 18445-18449.

(88) Grela, M. A.; Colussi, A. J. *J Phys Chem-Us* **1996**, *100*, 18214-18221.

(89) Tamaki, Y.; Furube, A.; Murai, M.; Hara, K.; Katoh, R.; Tachiya, M. *J Am Chem Soc* **2006**, *128*, 416-417.

(90) Chen, X.; Mao, S. S. *Chem Rev* **2007**, *107*, 2891-2959.

(91) Oskam, G.; Nellore, A.; Penn, R. L.; Searson, P. C. *J Phys Chem B* **2003**, *107*, 1734-1738.

(92) Sugimoto, T.; Okada, K.; Itoh, H. *J Colloid Interf Sci* **1997**, *193*, 140-143.

(93) Sugimoto, T.; Zhou, X. P. *J Colloid Interf Sci* **2002**, *252*, 347-353.

(94) Sugimoto, T.; Zhou, X. P.; Muramatsu, A. *J Colloid Interf Sci* **2002**, *252*, 339-346.

(95) Sugimoto, T.; Zhou, X. P.; Muramatsu, A. *J Colloid Interf Sci* **2003**, *259*, 53-61.

(96) Sugimoto, T.; Zhou, X. P.; Muramatsu, A. *J Colloid Interf Sci* **2003**, *259*, 43-52.

(97) Miao, L.; Tanemura, S.; Toh, S.; Kaneko, K.; Tanemura, M. *J Cryst Growth* **2004**, *264*, 246-252.

(98) Lin, Y.; Wu, G. S.; Yuan, X. Y.; Xie, T.; Zhang, L. D. *J Phys-Condens Mat* **2003**, *15*, 2917-2922.

(99) Lee, S.; Jeon, C.; Park, Y. *Chem Mater* **2004**, *16*, 4292-4295.

(100) Qiu, J. J.; Yu, W. D.; Gao, X. D.; Li, X. M. *Nanotechnology* **2006**, *17*, 4695-4698.

(101) Yang, J.; Mei, S.; Ferreira, J. M. F. *Mat Sci Eng C-Bio S* **2001**, *15*, 183-185.

(102) Chae, S. Y.; Park, M. K.; Lee, S. K.; Kim, T. Y.; Kim, S. K.; Lee, W. I. *Chem Mater* **2003**, *15*, 3326-3331.

(103) Zhang, Q. H.; Gao, L. *Langmuir* **2003**, *19*, 967-971.

(104) Feng, X. J.; Zhai, J.; Jiang, L. *Angew Chem Int Edit* **2005**, *44*, 5115-5118.

(105) Armstrong, A. R.; Armstrong, G.; Canales, J.; García, R.; Bruce, P. G. *Adv Mater* **2005**, *17*, 862-865.

(106) Wei, M. D.; Konishi, Y.; Zhou, H. S.; Sugihara, H.; Arakawa, H. *Chem Phys Lett* **2004**, *400*, 231-234.

(107) Kasuga, T.; Hiramatsu, M.; Hoson, A.; Sekino, T.; Niihara, K. *Langmuir* **1998**, *14*, 3160-3163.

(108) Du, G. H.; Chen, Q.; Che, R. C.; Yuan, Z. Y.; Peng, L. M. *Appl. Phys. Lett.* **2001**, *79*, 3702-3704.

(109) Wang, Y. Q.; Hu, G. Q.; Duan, X. F.; Sun, H. L.; Xue, Q. K. *Chem Phys Lett* **2002**, *365*, 427-431.

(110) Li, X. L.; Peng, Q.; Yi, J. X.; Wang, X.; Li, Y. D. *Chem-Eur J* **2006**, *12*,

2383-2391.

(111) Wen, B. M.; Liu, C. Y.; Liu, Y. *Inorg Chem* **2005**, *44*, 6503-6505.

(112) Wen, B. M.; Liu, C. Y.; Liu, Y. *New J Chem* **2005**, *29*, 969-971.

(113) Seifried, S.; Winterer, M.; Hahn, H. *Chem Vapor Depos* **2000**, *6*, 239-244.

(114) Pradhan, S. K.; Reucroft, P. J.; Yang, F. Q.; Dozier, A. *J Cryst Growth* **2003**, *256*, 83-88.

(115) Park, D. G.; Burlitch, J. M. *Chem Mater* **1992**, *4*, 500-502.

(116) Gurav, A.; Kodas, T.; Pluym, T.; Xiong, Y. *Aerosol Sci Tech* **1993**, *19*, 411-452.

(117) Oh, S. M.; Ishigaki, T. *Thin Solid Films* **2004**, *457*, 186-191.

(118) Wu, J. M.; Shih, H. C.; Wu, W. T. *Chem Phys Lett* **2005**, *413*, 490-494.

(119) Gong, D.; Grimes, C. A.; Varghese, O. K.; Hu, W. C.; Singh, R. S.; Chen, Z.; Dickey, E. C. *J Mater Res* **2001**, *16*, 3331-3334.

(120) Bauer, S.; Kleber, S.; Schmuki, P. *Electrochem Commun* **2006**, *8*, 1321-1325.

(121) Zuo, F.; Wang, L.; Wu, T.; Zhang, Z. Y.; Borchardt, D.; Feng, P. Y. *J Am Chem Soc* **2010**, *132*, 11856-11857.

(122) unpublished results.

(123) Zuo, F.; Bozhilov, K.; Dillon, R. J.; Wang, L.; Smith, P.; Zhao, X.; Bardeen, C.; Feng, P. *Angewandte Chemie International Edition* **2012**, *51*, 6223-6226.

Chapter 2

Self-doped Ti^{3+} Enhanced Photocatalyst For Hydrogen Production Under Visible-light

2.1 Introduction

Driven by increasing energy needs, decreasing fossil fuel resources and environmental concerns of nuclear energy, the search for clean and renewable energy is attracting massive research interest. Utilization of solar energy to produce hydrogen gas from water has long been considered an ultimate solution. Since the discovery in 1971 that TiO_2 acts as a photochemical water-splitting catalyst,[1] over 100 photocatalysts have been reported.[2] Because of its abundance, nontoxicity and stability, TiO_2 has been extensively studied. However, for practical applications, pure TiO_2 is not a good candidate, because it is only active under ultraviolet (UV) irradiation in order to overcome the bandgap of 3.2 eV for anatase phase. Therefore, bandgap engineering is required if we want to use TiO_2 as a water-splitting catalyst under visible light irradiation. Initially, cations such as Al, Nd, Sb, Ag, Ru, V, Cr, Mn, Fe, and etc. were used as dopants to introduce states into the TiO_2 bandgap.[3] However, problems like thermal instability, increased carrier recombination centers, and the need for an expensive ion-implantation facility pose significant limitations for this strategy.[4] Asahi claimed that doping nitrogen into TiO_2 is a better choice compared to doping with cations or other

anions.[4] However, later studies, both theoretically and experimentally have raised questions about this strategy and the suitability of the N-doping method as the most efficient method.[5] Furthermore, the reported activity for the photoreduction of water to hydrogen is quite low.[6]

Reduced TiO_2 (TiO_{2-x}), which contains the Ti^{3+} or oxygen vacancy, has been demonstrated to exhibit visible light absorption.[7] It was believed that the introduced localized oxygen vacancy states with energies 0.75 to 1.18 eV below the conduction band minimum of TiO_2 are lower than the redox potential for hydrogen evolution, which in combination with the low electron mobility in the bulk region due to this localization, makes the photocatalytic activity of the reduced TiO_2 negligible.[8] However, theoretical calculations show that a high vacancy concentration could induce a vacancy band of electronic states just below the conduction band.[3] The relevant experiments also prove the improved activity of reduced TiO_2 under visible light.[3] Therefore, these results demonstrate that it is possible to fabricate visible-light responsive TiO_2 by introducing Ti^{3+}.

The reported methods to produce TiO_{2-x} include heating TiO_2 under vacuum or reducing conditions (e.g. H_2), chemical vapor deposition, and high energy particle (laser, electron, or Ar^+) bombardment.[5] For practical application, these strategies have a number of limitations such as multiple steps, harsh synthesis conditions, or expensive facilities.

Furthermore, the surface oxygen defects are usually not stable enough in air as the Ti^{3+} is easily oxidized, and is even susceptible to oxidation by dissolved oxygen in water.[9-10] Therefore, developing a simple and economic strategy to synthesize a stable reduced TiO_2 photocatalyst is still a great challenge, which may be one reason why very limited studies have been reported for TiO_{2-x} photocatalyic activity, especially photocatalytic water-splitting.

Here we report a one-step method to synthesize reduced TiO2, which exhibits extremely high stability and is active for photocatalytic hydrogen production from water.

2.2 Experimental Section

2.2.1 Synthesis Method

All chemicals, including ethyl alcohol (Gold shield, 200 proof), 2-ethylimidazole (Aldrich, 98%), titanium (IV) isopropoxide (Acros, 98+%), and hydrochloric acid (Fisher scientific, 37.1%), were used as received without any further purification.

In a typical synthetic procedure, ethanol (10.00g), 2-ethylimidazole (1.80g), and hydrochloric acid (2.50g) were mixed in a 50-mL pyrex beaker and magnetically stirred for 15 minutes to get a clear solution. Then titanium (IV) isopropoxide (2.00g) was added to the beaker dropwisely and stirred for another 15 minutes. The beaker was then placed

into a preheated oven (500 °C) to undergo combustion. After 5 hours reaction time, the final product was obtained, with no further purification.

2.2.2 Characterization

Powder X-ray diffraction data were collected using a Bruker D8-Advance powder diffractometer operating at 40kV, 40mA for Cu Kα radiation (λ=1.5406 Å).

The EPR spectra were recorded on a Bruker EMX EPR spectrometer at an X-band frequency of 9.363 GHz, sweep width of 500.00 Gauss, and center field of 3390.00 Gauss.

The UV-visible absorption spectra were recorded on a Shimadzu UV-3101PC UV-Vis-NIR spectrophotometer operating in the diffuse mode with application of the Kubelka-Munk equation.

The elemental analysis was performed by the MSI Analytical Lab at the University of California Santa Barbara.

Photocatalytic H_2 production experiments were conducted in a sealed circulation system. 1% Pt was load as a cocatalyst by UV irradiation of $PtCl_4$ aqueous solution. In a typical run, 0.300g of sample was suspended in 120 mL 25% methanol aqueous solution (containing 0.005 $PtCl_4$) under magnetic stirring. Then a 300 W Xe lamp was applied to this mixture for 30 minutes, in that case, the Pt nanoparticles would be loaded to the surface of TiO_2 as cocatalyst under the UV irradiation. After degassing the system

for one hour, this 300 W Xe lamp with a 400 nm cut-on filter (Newport Corp.) was applied to execute the photocatalytic reaction. The products were analyzed by gas chromatography (Shimadzu GC-8A) equipped with a thermal conductivity detector (TCD).

The external quantum efficiency (EQE) was calculated based on the equation: EQE= 2H/P. Here H was the number of moles of hydrogen gas produced during a specific time, while P was the number of photons incident on the photocatalytic system within the same time period. To measure the average EQE in the range of 400 nm to 455 nm, a 400 nm cut-on filter and a 455 nm cut-off filter were used. For measurement of the EQE at 420 nm, a 420 nm bandpass filter (Newport Corp.) was used. The number of the incident photons was determined using a radiant power energy meter (Newport Corp., Model 70260 with a Thermopile Detector).

2.3 Results and Discussion

2.3.1 Structural Analysis

The powder X-Ray diffraction analysis (Figure 1) shows that the as-produced sample is a mixture of anatase phase and rutile phase TiO_2.

To test for the presence of Ti^{3+} low temperature electron paramagnetic resonance (EPR) spectra were recorded (Figure 2). The as-synthesized sample gave rise to a very strong EPR signal, while no signal was seen for the commercial Dequssa P25 (a mixture

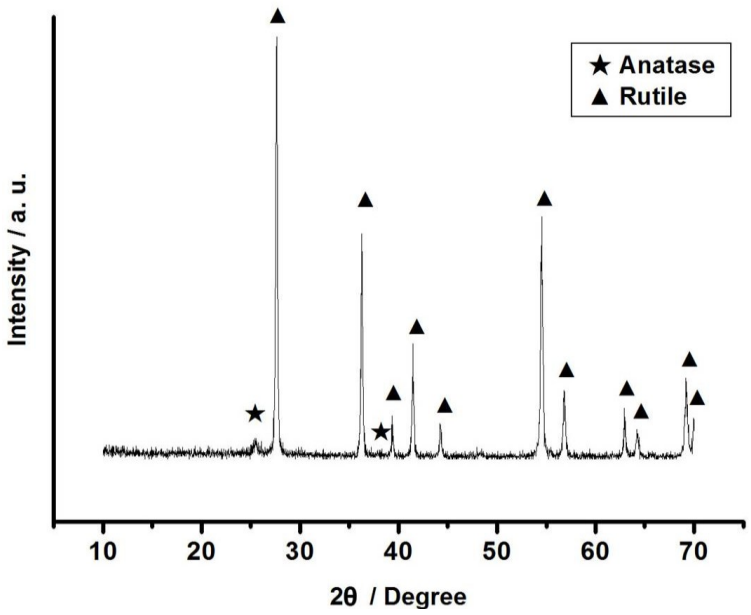

Figure 1. XRD patterns for as-prepared samples through combustion in air of the ethanol solution of Titanium (IV) isopropoxide, and 2-ethylimidazole at 500 °C and kept in the oven for 5 hours.

of anatase and rutile TiO_2, Figure 3). Anisotropic powder pattern g-values of $g_x=g_y=1.975$ and $g_z=1.944$ were obtained from a simulation that yielded a near perfect fit to the data. Note that test temperature shows a strong effect on the EPR peak shapes. When T is below 100K, the anisotropic g tensors will be a narrowing of the lines with decreasing temperature. When T is above 100K, the anisotropy of g is greatly attenuated. The observed g-values are characteristics of a paramagnetic Ti^{3+} center in a distorted rhombic oxygen ligand field.[11] The EPR data also indicate that there is no Ti^{3+} present on the surface of the sample. It is believed that surface Ti^{3+} would tend to adsorb atmospheric O_2, which would be reduced to O_2^- and shows an EPR signal at g~2.02.[12] The absence of such a peak in Figure 1A would indicate that only the rhombic Ti^{3+} is

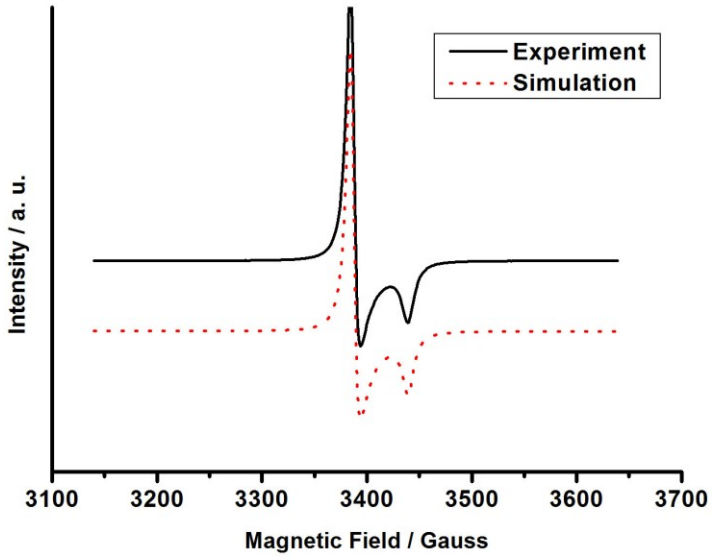

Figure 2. Experimental (solid line, measured under 75K) and simulated (dashed line) EPR spectra for sample.

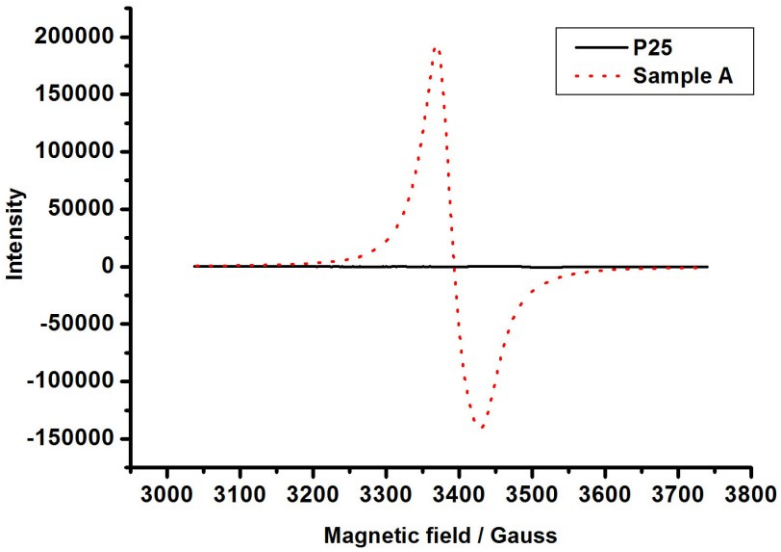

Figure 3. EPR spectra for commercial P25 and sample. The spectra are recorded at 100K. At this temperature the anisotropic g tensors for sample are not resolved.

present in the bulk, which is a key factor in the observed excellent stability of our sample.

Furthermore, P25 shows no EPR signal, meaning neither pure anatase nor pure rutile can

account for the EPR peaks observed in sample. From this information we conclude that Ti^{3+} is present in sample, and that only rhombic Ti^{3+} exists in the bulk. Surface analysis of sample using X-ray photoelectron spectroscopy (XPS) shows no Ti^{3+} peaks and further confirms the conclusion that Ti^{3+} exists in the bulk.

2.3.2 Proposed Chemical Reactions

$$Ti(OC_3H_7)_4 + 4H_2O \longrightarrow Ti(OH)_4 + 4C_3H_8O$$

$$Ti(OH)_4 \xrightarrow{\Delta} TiO_2 + 2H_2O$$

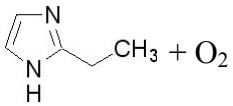

$$+ O_2 \longrightarrow CO + CO_2 + NO + NO_2$$

$$TiO_2 + CO \longrightarrow TiO_{2-x} + CO_2$$

$$TiO_2 + NO \longrightarrow TiO_{2-x} + NO_2$$

2.3.3 UV-vis Absorption Spectra

Figure 4 shows the UV-visible absorption spectra for sample and the commercial anatase. The spectrum for sample shifts to longer wavelength revealing a decrease in the bandgap. Meanwhile, the absorbance in the visible range is enhanced compared to the stoichiometric anatase. This phenomenon is consistent with the assumption that an electronic band is located just below the conduction band of pure TiO_2.

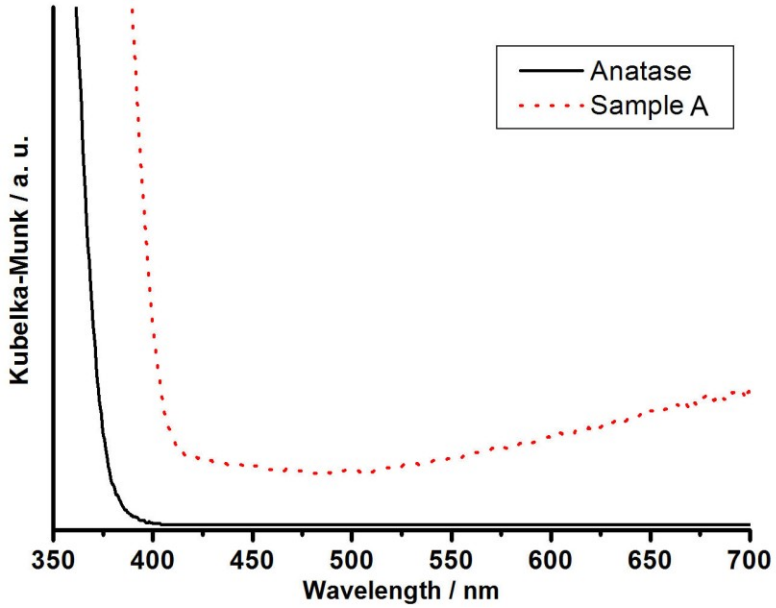

Figure 4. UV-Visible diffuse reflectance spectra for commercial anatase TiO_2 (solid line) and sample (dash line).

2.3.4 Theoretical Calculation

Theoretical simulation using PWscf package[13] was executed to support the existence of a Ti^{3+} induced electronic band and to further understand its likely influence on the band structure of oxygen deficient TiO_2. The calculations, based on plane wave pseudopotential density functional theory (DFT) approach, were performed on 1×1×2 and 2×2×1 anatase supercell with one O atom removed from each system in order to simulate different concentration of Ti^{3+}. The plane-wave basis set with energy cutoff of 30 Ryd was satisfactory for ultrasoft pseudopotential with PBE (Perdew-Burke-Ernzerhof) exchange correlations to capture the properties of anatase phase. Brillouin-zone integration was computed with k points in a Monkhorst-Pack (10, 10, 5) grid. We see a

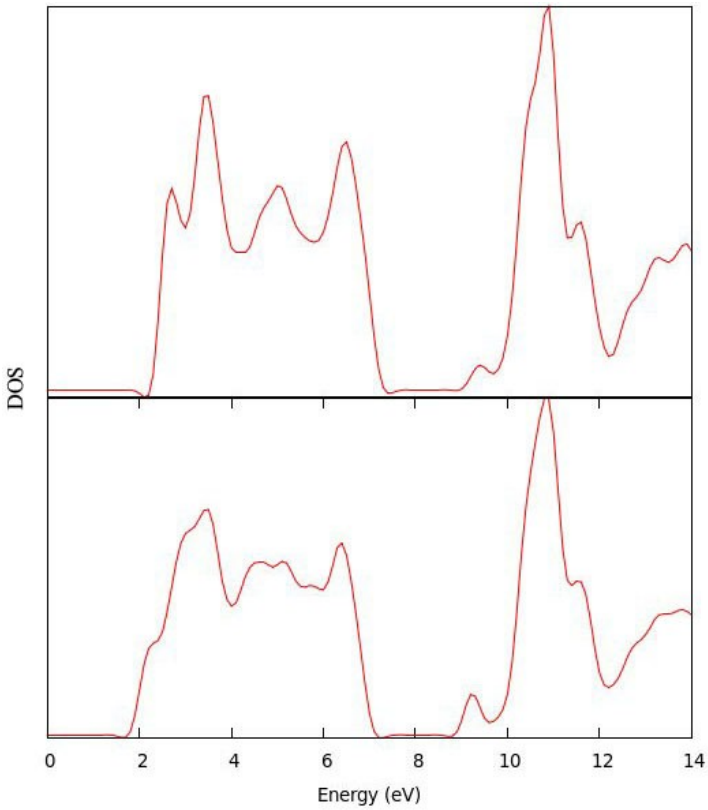

Figure 5. Calculated density of electronic states (DOS) for anatase. Upper curve is the DOS for the structure with 1 O vacancy per 32 O atoms, while the lower curve is for the one with 1 O vacancy per 16 O atoms.

miniband rising up closely below the conducting band minimum (Figure 5). It is found that the width of the band is related to the concentration of the Ti^{3+} or oxygen vacancy, since the width increases as the concentration of oxygen vacancy increased from 1 per 32 to 1 per 16 oxygen atoms. Very similar results have also been reported by Figueras.[3] The above calculations proved that the Ti^{3+} inside the bulk TiO_2 is responsible for the bandgap narrowing. Furthermore, the presence of the vacancy band has been reported as an extra benefit for light absorption. The high concentration of oxygen vacancy could break the

selection rule for indirect transitions, resulting in an enhanced absorption for photon energy below the direct bandgap,[3] which has been observed in our UV-visible spectra.

2.3.5. H_2 Evolution Study

The photocatalytic activity of sample for water-reduction was studied in the following manner. After loading 0.300 g sample with 1% Pt (0.003 g),

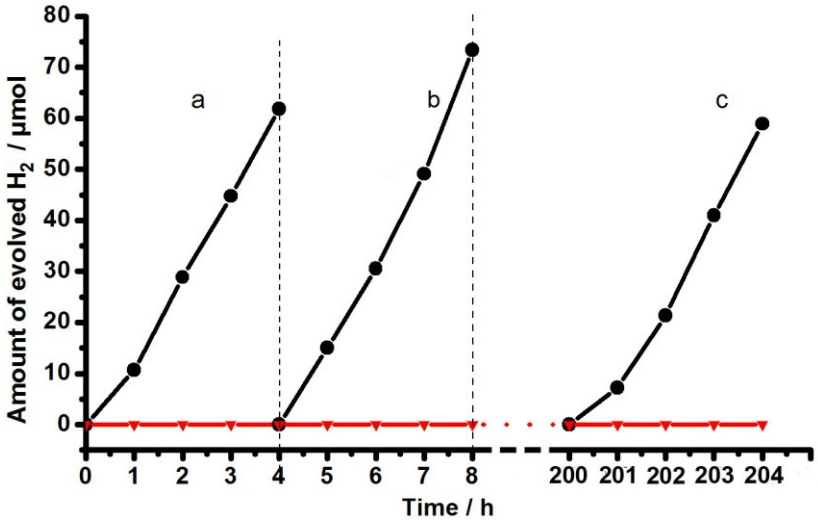

Figure 6. Time course of evolved H_2 under visible light (>400 nm) irradiation. a) reaction for 4 hours; b) evacuating and continue reaction for another 4 hours; c) illuminated for 200 hours, evacuating system and continue reaction for 4 hours. ●: Sample; ▼: Anatase

the photocatalyst was placed into a 120 ml 25% methanol (as a sacrificial agent) aqueous solution in a closed-gas circulation system**.** A Xe lamp (300 W) with a 400 nm cut-on filter was used to ensure that only visible light (>400 nm) illuminated the photocatalyst. Figure 6 shows a typical time course of H_2 evolution. This photocatalytic reaction exhibits a stable H_2 release rate at ~ 15 µmol/h/0.300g. Even after illumination for 200

hours, the activity is still maintained with no noticeable decrease observed, demonstrating the excellent stability of the sample. We also compared the EPR spectra for the sample before and after the long term (116h) visible light irradiation, and the intensity of the EPR spectra did not show decrease after the photocatalytic reaction as shown in Figure 7.

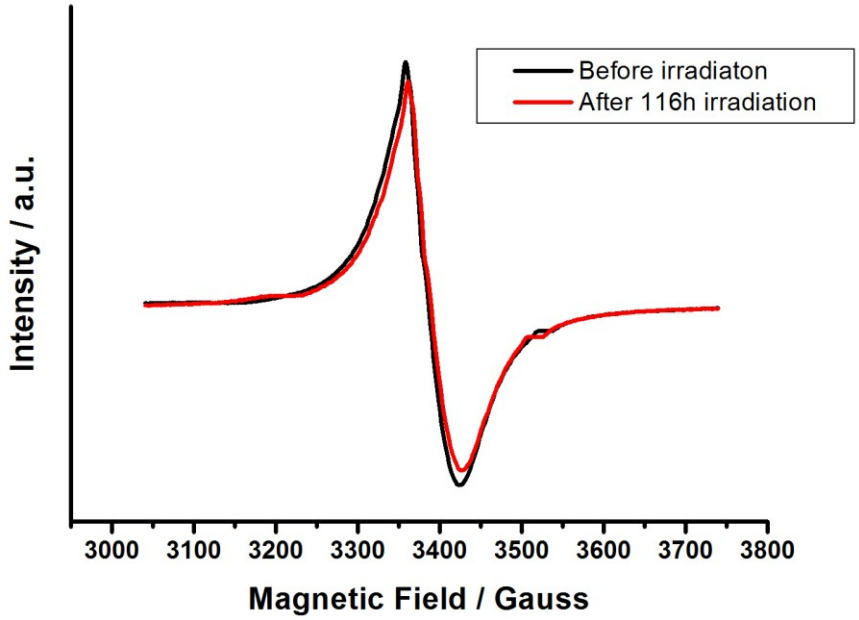

Figure 7. EPR spectra for sample measured before and after visible light irradiation at 100K.

To understand the solar energy conversion efficiency of the sample, the average external quantum efficiency (EQE) in the range of 400 nm – 455 nm was measured and found to be 0.79%. We further measured the EQE with a 420 nm band pass filter, which gave an EQE of 0.35%, consistent with the above result. The commercial anatase TiO_2 has also been studied for comparison. Although it exhibits a high activity under UV light, no

apparent H_2 peak appears under visible light (>400 nm) illumination for the anatase TiO_2, providing strong evidence for extending the photocatalytic activity to the visible light range through our strategy.

To exclude the influence of the nonmetal dopants, like nitrogen, we replace the 2-ethylimidazole with urea, and keep any other experimental parameters unchanged.

Table 1. Elemental Analyses

Sample ID	Weight (μg)	Weight percent (%)	
		C	N
Sample	62627	0.060	0.011
Sample *	49952	0.061	0.009
Sample X	60425	0.164	0.281
Sample X*	59283	0.159	0.279

* Repeated result for sample.
Sample: the sample synthesized from 2-ethylimidazole
Sample X: the controlled sample synthesized from urea.

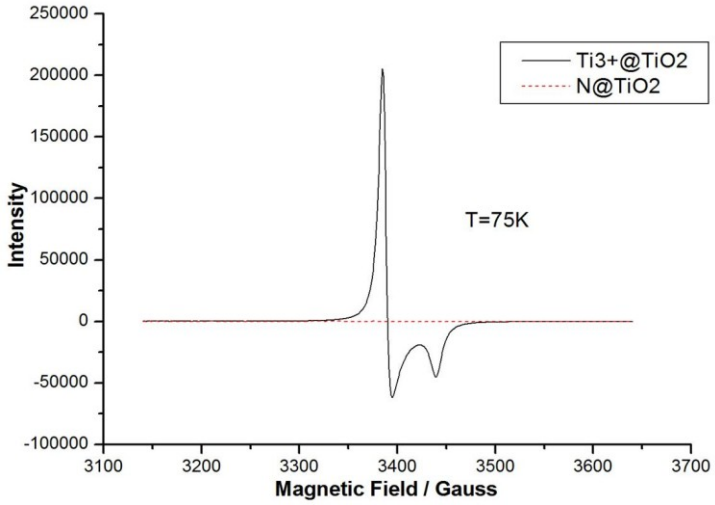

Figure 8. The EPR spectra for Ti^{3+}-doped sample and N-doped sample obtained at 75K.

The elemental analyses (Table 1) prove the presence of the N in the sample from urea. However, the EPR study shows no measurable Ti^{3+} existing in the N-doped TiO2 (Figure 8), and this sample shows almost no H_2 production activity under visible light illumination (<0.1μmol/h/0.300g). Also, the reported C-doped TiO_2 visible light water-splitting reaction requires photoeletrochemical reaction system and voltage bias[14], which are not necessary for our Ti^{3+} sample. Therefore, it is Ti^{3+} not C or N that is responsible for the visible light response. The controlled experiments further confirmed the effect of Ti^{3+}.

2.4 Conclusion

We have developed a simple one-step method to synthesize Ti^{3+} doped TiO_2. The as-prepared reduced TiO_2 exhibits high stability in air and water with light irradiation. Experimental data show a good conversion efficiency in the visible light region (>400 nm). Both theoretical calculations and experimental results support that it is the introduced Ti^{3+} that accounts for the extension of the photocatalytic activity from the UV light region to the visible light region. The present study demonstrates a simple and economical method for narrowing the bandgap and for the development of a highly active photocatalyst under visible light irradiation.

2.5 References

(1) Fujishima, A.; Honda, K. *B. Chem Soc Jpn* **1971**, *44*, 1148.

(2) Osterloh, F. E. *Chem Mater* **2008**, *20*, 35.

(3) Justicia, I.; Ordejon, P.; Canto, G.; Mozos, J. L.; Fraxedes, J.; Battiston, G. A.; Gerbasi, R.; Figueras, A. *Adv Mater* **2002**, *14*, 1399.

(4) Asahi, R.; Morikawa, T.; Ohwaki, T.; Aoki, K.; Taga, Y. *Science* **2001**, *293*, 269

(5) Thompson, T. L.; Yates, J. T. *Chem Rev* **2006**, *106*, 4428.

(6) Kim, H. G.; Hwang, D. W.; Lee, J. S. *J Am Chem Soc* **2004**, *126*, 8912.

(7) Sasikala, R.; Shirole, A.; Sudarsan, V.; Sakuntala, T.; Sudakar, C.; Naik, R.; Bharadwaj, S. R. *Int J Hydrog Energy* **2009**, *34*, 3621.

(8) Cronemeyer, D. C. *Phys Rev* **1959**, *113*, 1222.

(9) Teleki, A.; Pratsinis, S. E. *Phys Chem Chem Phys* **2009**, *11*, 3742.

(10) Komaguchi, K.; Maruoka, T.; Nakano, H.; Imae, I.; Ooyama, Y.; Harima, Y. *J Phys Chem C* **2010**, *114*, 124.

(11) Khomenko, V. M.; Langer, K.; Rager, H.; Fett, A. *Phys Chem Miner* **1998**, *25*, 338.

(12) Anpo, M.; Che, M.; Fubini, B.; Garrone, E.; Giamello, E.; Paganini, M. C. *Top Catal* **1999**, *8*, 189.

(13) Baroni, S.; Dal Corso, A.; de Gironcoli, S.; Giannozzi, P. http://www.pwscf.org.

(14) Khan, S. U. M.; Al-Shahry, M.; Ingler, W. B. *Science* **2002**, *297*, 2243.

Chapter 3

Self-Doped Ti^{3+}@TiO_2 Visible Light Photocatalyst: Influence of Synthetical Parameters on the H_2 Production Activity

3.1 Introduction

We have reported that Ti^{3+} could be introduced to partially reduced TiO_2 by using a facile one-step combustion method.[1] It is found that Ti^{3+} extends the photoresponse of TiO_2 from the UV to the visible light region, which leads to high visible-light photocatalytic activity for the generation of hydrogen gas from water. This extension of the light absorption is proposed to originate from a miniband rising up closely below the conducting band minimum of regular TiO_2. Unlike the common conception that the surface Ti^{3+} tends to adsorb atmospheric oxygen and so oxidized to Ti^{4+},[2,3] the Ti^{3+} present in the bulk of our sample shows an excellent stability in air and water under light irradiation.

It is well accepted that the synthetic conditions will greatly affect the physical properties such as crystallinity, surface area, particle size, crystal facets distribution and etc. of the products and finally results in significant different activity for photocatalysts.[4-7] So it is worthy to further research what impacts will be imposed to the photocatalytic activity of as-prepared reduced TiO_2 under various preparation parameters.

Herein, we study in detail the relationships between the physical properties and the amount of the imidazole used as the starting material. It is found that dosage of the imidazole has a great effect on the phase composition, UV-vis absorption, surface area of the products, as well as the photocatalytic activity. The influence of the various imidazoles and Ti sources is also studied. Upon the research of this synthetic condition-photocatalytic activity relationship, we could expect to further understand the process of the photocatalytc reaction and improve the activity.

3.2 Experimental Section

3.2.1 Synthesis of Various Ti^{3+} Doped TiO_2

10.00 g ethanol (Gold shield, 200 proof), 0.1-2.5 g 2-ethylimidazole (Aldrich, 98%), and 2.5 g hydrochloric acid (Fisher scientific, 37.1%) were mixed in a 50-mL pyrex beaker and magnetically stirred for 15 minutes to get a clear solution. Then 2.00 g titanium (IV) isopropoxide (TTIP, Acros, 98+%) was added to the beaker dropwisely and stirred for another 15 minutes. The beaker was then placed into a preheated oven (500 °C) to undergo combustion. After 5 hours reaction time, the final product was obtained, with no further purification.

3.2.2 Load Cocatalyst

The loading of Pt cocatalyst was performed through a popular photodecomposition stragety,[8-11] i.e. 1% Pt was load as a cocatalyst by UV irradiation of $PtCl_4$ aqueous

solution. In a typical run, 0.100g of sample was suspended in 120 mL 25% methanol aqueous solution (containing 0.005 $PtCl_4$) under magnetic stirring. A 300 W Xe lamp was applied to this mixture for 30 minutes, the Pt nanoparticles would be loaded to the surface of TiO_2 as cocatalyst under the UV irradiation.

3.2.3 Photocatalytic Reaction Test

After transferring the above mixture to a sealed circulation system and degassing for one hour, the 300 W Xe lamp with a 400 nm cut-on band pass filter (Newport Corp.) was applied to execute the photocatalytic reaction. The products were analyzed by gas chromatography (Shimadzu GC-8A) equipped with a thermal conductivity detector (TCD).

3.2.4 Quantum Efficiency Measurement

The external quantum efficiency (EQE) was calculated based on the equation: EQE= 2H/P. Here H was the number of moles of hydrogen gas produced during a specific time, while P was the number of photons incident on the photocatalytic system within the same time period. To measure the average EQE in the range of 400 nm to 455 nm, a 400 nm cut-on filter and a 455 nm cut-off filter were used. For measurement of the EQE at 420 nm, a 420 nm bandpass filter (Newport Corp.) was used. The number of the incident photons was determined using a radiant power energy meter (Newport Corp., Model 70260 with a Thermopile Detector).

3.2.5 Characterization

Powder X-ray diffraction data were collected using a Bruker D8-Advance powder diffractometer operating at 40kV, 40mA for Cu Kα radiation (λ=1.5406 Å). The EPR spectra were recorded on a Bruker EMX EPR spectrometer at an X-band frequency of 9.363 GHz, sweep width of 500.00 Gauss, and center field of 3390.00 Gauss. The UV-visible absorption spectra were recorded on a Shimadzu UV-3101PC UV-Vis-NIR spectrophotometer operating in the diffuse mode with application of the Kubelka-Munk equation. The elemental analysis was performed by the MSI Analytical Lab at the University of California Santa Barbara. BET test are performed by ASAP 2020 (Micromeritics).

3.3 Results and Discussion

3.3.1 Crystal Structure and Phase Composition Analysis

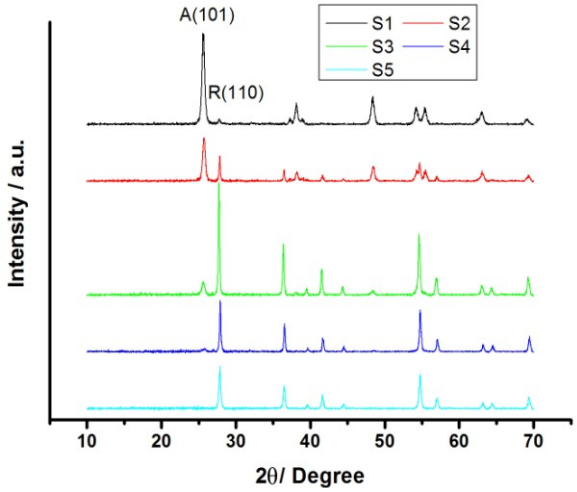

Figure 1. XRD patterns for the products S1, S2, S3, S4 and S5 synthesized from 0.1g, 0.3g, 1.0g, 1.8g and 2.5g of 2-ethylimidazole, respectively.

The XRD patterns of the samples (Figure 1) showed that they are mixtures of anatase and rutile phase. As the amount of 2-ethylimidazole increasing, the proportion of rutile phase goes up. It is reported that in the mixture of rutile and anatase, the weight percentage of rutile (W_R) can be determined by the following the equation:[12,13]

$$W_R = \frac{A_R}{0.884A_A + A_R}$$

Here, the A_R stands for the integrated intensity of rutile (110) peak, and the A_A for the integrated intensity of anatase (101) peak.

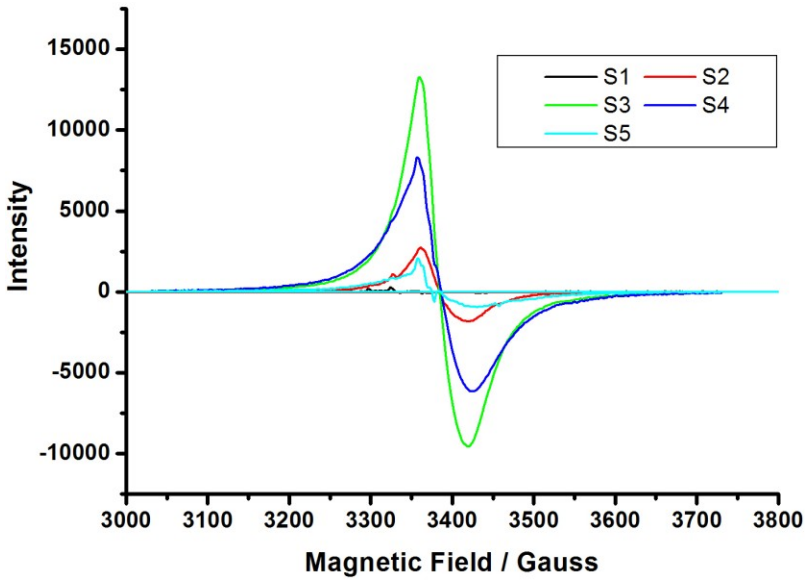

Figure 2. EPR spectra for S1-S5 under 100K.

When 0.1 g 2-ethylimidazole was used, the sample contains 94.7% anatase, and 5.3% rutile, as the 2-ethylimidazole increase to 2.5g, the percentage of rutile increase to 96.7%, only trace amount of anatase remaining in the sample. The details for phase compostion are summarized in Table 1. These phase composition analysis shows that the

2-ethylimidazole is favorable for the growth of rutile. One possible explanation for this phenomenon could be the temperature factor. When more 2-ethylimidazole (fuel) is introduced into the combustion system, the temperature of the combustion reaction is higher, which would result in more rutile phase formed, as it is well known that rutile phase is more stable than anatase phase under high temperature (>500 °C).

3.3.2 Ti^{3+} Characterization

EPR measurements of these samples demonstrate the presence of Ti^{3+} in all the above samples. However, unlike the phase composition, which shows a simple proportional to the amount of 2-ethylimidazole, the concentration of Ti^{3+} does not always raise as the usage of 2-ethylimidazole increase. In the earlier range (0.1g-2.5g 2-ethylimidazole), the concentration of Ti^{3+} is increasing as 2-ethylimidazole goes up. When the 2-ethlyimidazole comes to 3.0g, the Ti^{3+} decrease. We have proposed that in the oven, a fast combustion could convert the 2-ethylimidazole to NO, NO_2, and CO, which are powerful reducing agents to reduce the Ti^{4+} to Ti^{3+}.

$$Ti(OC_3H_7)_4 + 4H_2O \longrightarrow Ti(OH)_4 + 4C_3H_8O$$

$$Ti(OH)_4 \xrightarrow{\Delta} TiO_2 + 2H_2O$$

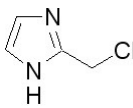

$$+ O_2 \longrightarrow CO + CO_2 + NO + NO_2$$

$$TiO_2 + CO \longrightarrow TiO_{2-x} + CO_2$$

$$TiO_2 + NO \longrightarrow TiO_{2-x} + NO_2$$

With more 2-ethylimidazole is combusted, more reducing gases will be procued, and so more Ti^{3+} are formed. However, as we mentioned before, the combustion temperature is also increased, and some Ti^{3+} will be converted back to Ti^{4+} under high temperature, which have been observed by our controlled experiments. When we heat up the as-synthesized partially reduced TiO_2 to 700 or 800 degree, the color will slowly turn into white, and the EPR peak for Ti^{3+} gradually disappears. This factor could be a reason why excessive 2-ethylimidazole is detrimental to the formation of Ti^{3+}. Here the order of the concentration of Ti^{3+} presence in the as-synthesized products is: S3>S4>S2>S5>S1. It is worth noting that even the S3 has the highest concentration of Ti^{3+}, it is not the most active photocatalyst, which will be discussed in the later section.

3.3.3 Optical Absorption Study

The UV-Vis spectra are collected on all the prepared samples and shown in Figure 3. Among these samples, the S1 shows the lowest absorption at visible light range (>400nm). From S2 to S4, these samples exhibit enhanced visible light absorption. Considering that these samples contain more Ti^{3+} than S1, therefore we could conclude that that Ti^{3+} is favorable for the visible light absorption. It is worthy to note that S4 exhibits the highest visible light absorption compared to the other four samples, either at

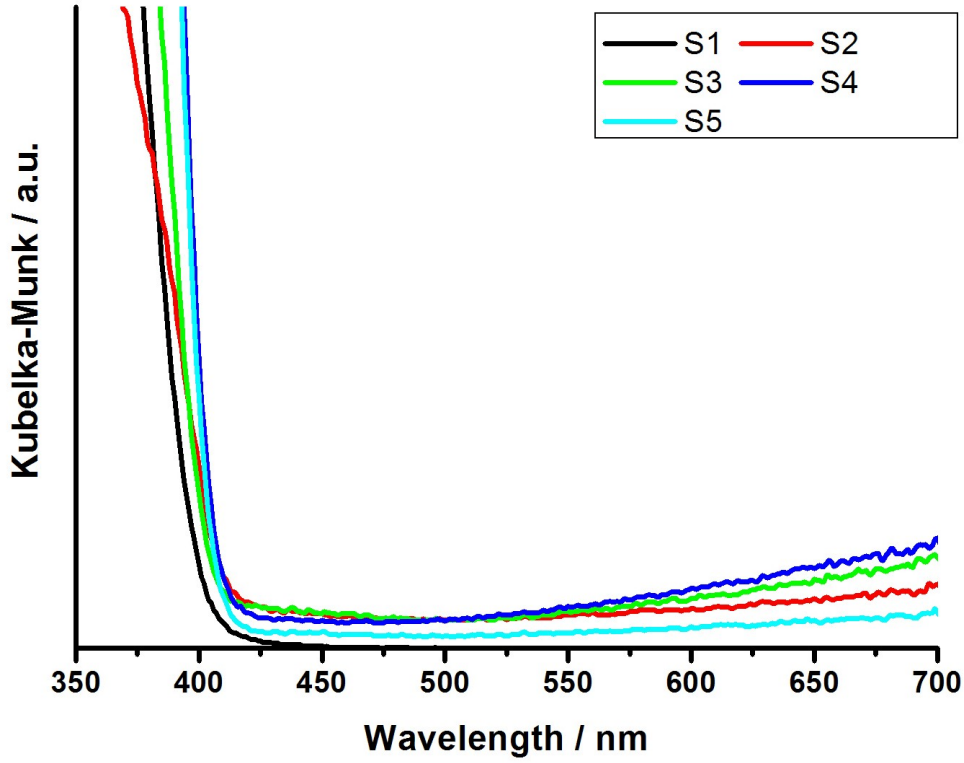

Figure 3. UV-Visible diffuse reflectance spectra for S1- S5.

the point of 400 nm or within the range from 400 to 700 nm. Our theoretical calculation has proved that there will be a miniband forming right below the conducting band minimum of stoichiometric TiO_2 (Figure 4). The miniband may work as both donor levels and acceptor levels. These theoretical calculations demonstrated that the Ti^{3+} inside the bulk TiO_2 is responsible for the band gap narrowing. Moreover, the enhanced visible light absorption after 400 nm in the samples S2 to S4 could be ascribed to the high concentration of oxygen vacancy, which could form a vacancy band and break the selection rule for indirect transitions, resulting in an enhanced absorption.

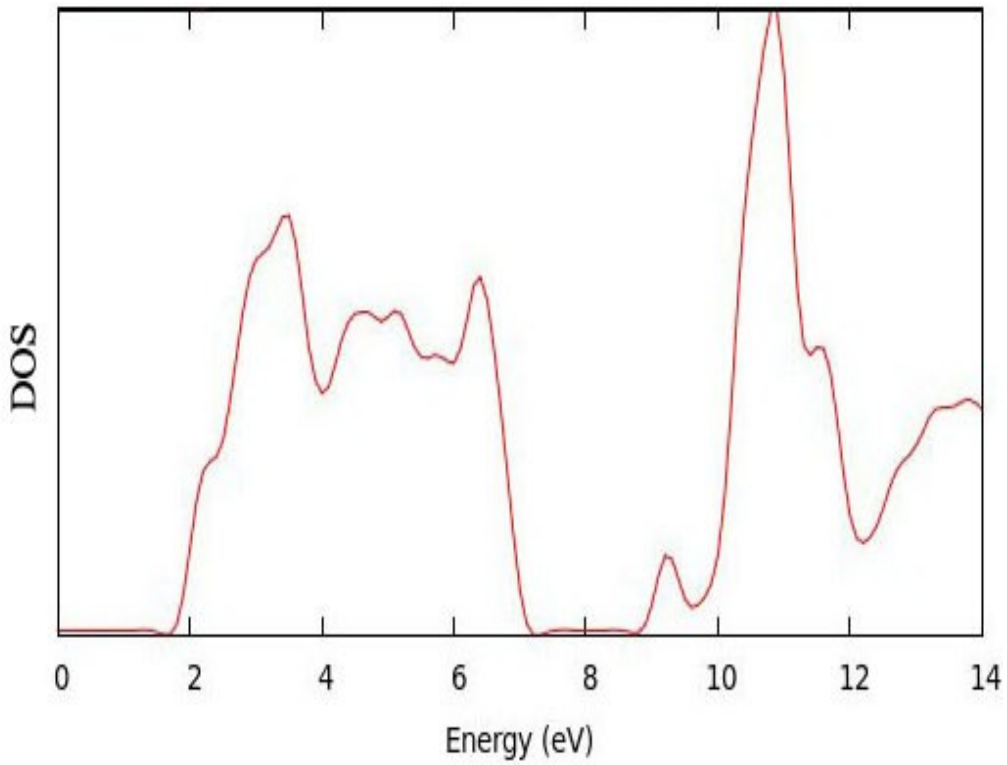

Figure 4. Calculated density of electronic states (DOS) for anatase phase TiO2 with 1 O vacancy per 16 O atoms.

3.3.4 Specific surface area measurements

It is well known that surface area is a key factor for photocatalytic activity. With large specific surface area, the photocatalysts will offer more reactive sites, so improving

Table 1. Summary of chemical and physical properties for S1-S5.

Sample	Amount of 2-ethylimidazole (g)	Rutile%	Anatase%	Surface area (m^2/g)	Particle size (nm)	H2 evolution rate (μmol/h/0.3g)
S1	0.1	5.3	94.7	56.83	60	0.61
S2	0.3	24.7	75.3	27.86	80	1.52
S3	1.0	82.4	17.6	18.96	130	2.67
S4	1.8	88.9	11.1	11.72	160	14.82
S5	2.5	96.7	3.3	11.01	170	8.07

the photocatalytic reaction rate, as well as the efficiency for solar energy conversion. Basing on this consideration, we studied the BET surface area of the above samples. The results are summarized in Table 1. It is obviously that the surface area shrinks if more 2-ethylimidazole is adding to the reaction system. The reason for this phenomenon is easy to understand: when introducing more fuel into the combustion process, the plenty of heat released will make the product collapse and dense structure will be formed. That why the as-synthesized sample from 0.1g 2-ethylimidazole have large surface area of 58.8 m^2/g, while 1.8 and 2.5 g 2-ethylimidazole result in the surface area shrinking into ~ 10 m^2/g.

3.3.5 Morphology Study

SEM images show that these as-prepared $Ti^{3+}@TiO_2$ are nanoparticles, and the particle size is within 60-170 nm range. Low dose of 2-ethylimidazole gives birth to the small nanoparticles with ~60 nm in diameter (Figure 5a), while high dose of 2-ethylimidazole results in larger nanoparticles with diameter of ~ 170 nm (Figure 5e). This SEM observation is well consistent with the BET measurements, i.e. as more dose of fuel used, the small nanoparticles tend to fuse into bigger ones, and so decreases the surface area. Figure 5f is the typical TEM image of S4, which further proves the size of the nanoparticles, and agrees with the SEM results well.

3.3.6 Visible Light Photocatalytic Activity

After loading 1% (wt) Pt on the surface of the reduced TiO_2, 0.1g sample is placed into a gas-closed circulation system. We study the H_2 evolved rate in

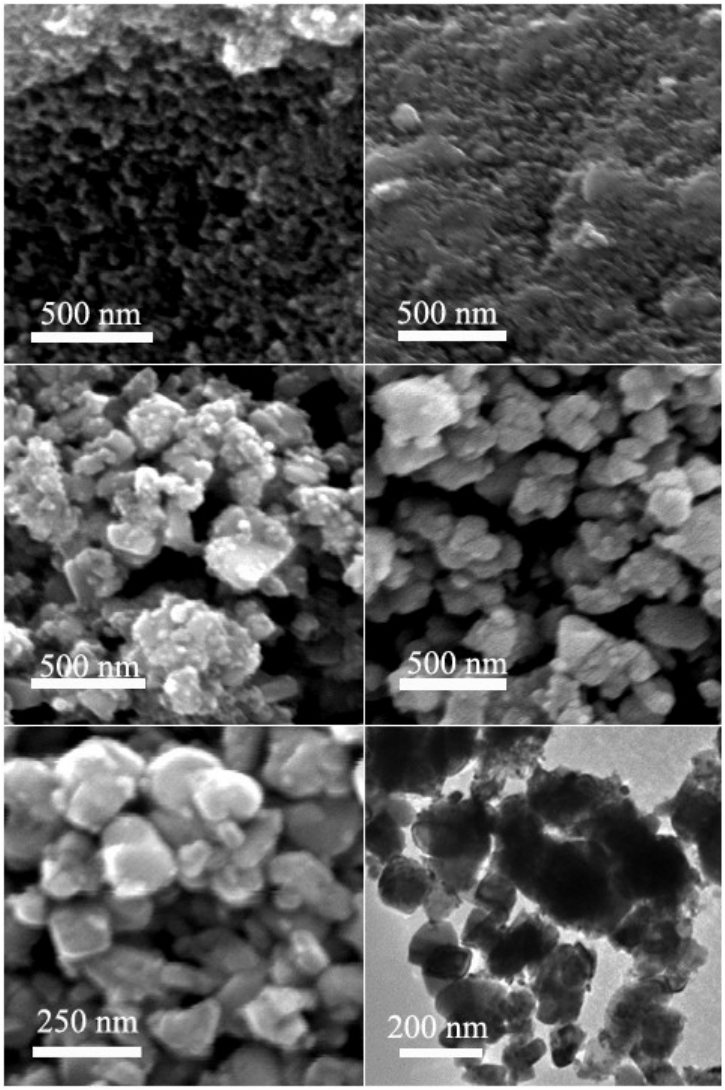

Figure 5. a), b), c), d), e) are the SEM images for S1, S2, S3, S4, and S5, respectively. f) is the TEM image for S4.

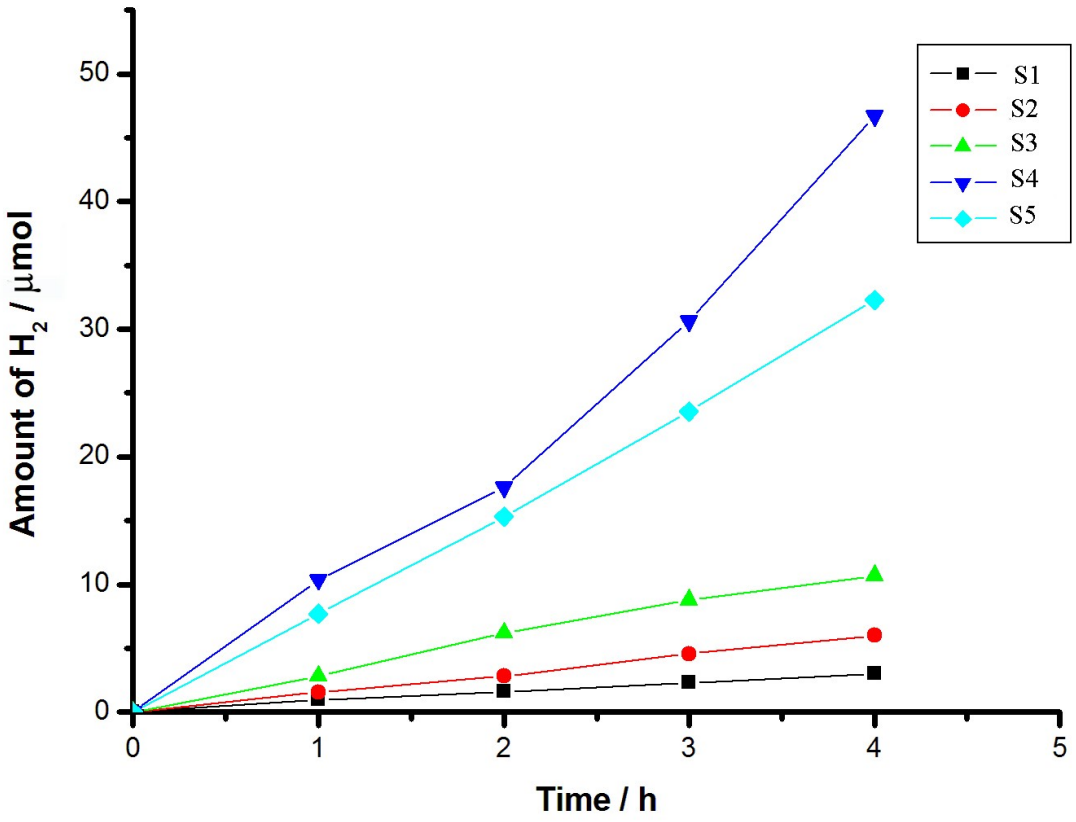

Figure 6. Time course of H_2 evolution for S1-S5.

the presence of 25% methanol as the sacrificial agent. The results are shown in Figure 6. It is not surprising that the S1 shows the lowest H_2 producing rate. The UV-Vis spectra have demonstrated that the absorption for S1 at wavelength greater than 400 nm is extremely weak, which means only a tiny amount of energy from the illumination of the lamp could be used to reduce water, so the H_2 evolving rate is as low as 0.61 μmol/h/0.1 g. As more 2-ethylimidazole is added to the reaction system, the products exhibit higher efficiency to convert the visible light energy to H_2, which could be understood from the

EPR and UV-Vis spectra results. From S1 to S3, the Ti^{3+} concentration hiked, as well as the visible light absorption, so it is not surprising that the H_2 evolving rate on the visible light region increases from S1 to S3. When the amount of 2-ethylimidazole reached 2.5 g, however, the H_2 release rate of S5 (7.7 μmol/h/0.1 g) decreased compared to that of S4 (14.82 μmol/h/0.1 g). Also, though S3 has a stronger EPR signal than S4, its H_2 producing rate (2.67 μmol/h/0.1g) is much lower than S4. This phenomenon could be explained by the UV-Vis absorption spectra. In the H_2 production experiment, we used a 400 nm cutoff bandpass filter. The absorption at 400 nm for S3 is only ~ 54% of absorption for S4. In addition, as discussed before, the crystallinity of the materials is another key factor for the activity. S4 is supposed to be better crystalline than S3 considering that more fuel is used for S4 so higher reaction temperature helps the sample S4 better crystallized than S3. This assumption is supported by our SEM results, which clear show that there are many small nanoparticles (~ 50 nm) surrounding the big crystals in S3, making the sample have a broad size distribution and seem rather rough (Figure 5c). In the case S4, it is mostly composed by large crystals (~ 170 nm) and surface look smooth (see Figure 5d and Figure 5f). For S5, the absorption within the 400 to 700 nm is much weaker than S4, so it is not as active as S4 in reducing water. Another possible reason for S5's lower activity is that some researcher have reported the produced electron-hole pairs in TiO_2 will be trapped as Ti^{3+} and surface hydroxyl radical,

respectively. Since S4 has a much higher Ti^{3+} concentration than S5, the lifetime of the excited electron in S4 is probably longer the that in S5, so improving the water reducing activity.

The influence of different Ti source was studied by replace the titanium isopropoxide with Ti(IV) n-butoxide and $TiCl_4$. The former show a moderated activity, and the later show no visible light activity. EPR measurement confirmed that there are no Ti^{3+} form in the case of $TiCl_4$, which support that the crucial role of Ti^{3+} for visible light activity.

3.4 Conclusion

After studying a series of products synthesized from different amount reducing agents and fuel by XRD, EPR, BET, SEM, and UV-vis, we found that phase composition, Ti^{3+} concentration, specific surface area, morphology, and light absorption are all affected by the amount of imidazole. Even though this affection is not strong for each single property, however, the photocatalytic activity is governed by the coordination among all the aspects, and which make the overall photocatalytic activity is sensitive to the dose of imidazole. We call this is a synergic effect.

3.5 References

(1) Zuo, F.; Wang, L.; Wu, T.; Zhang, Z. Y.; Borchardt, D.; Feng, P. Y. *J Am Chem Soc* **2010**, *132*, 11856-11857.

(2) Teleki, A.; Pratsinis, S. E. *Phys Chem Chem Phys* **2009**, *11*, 3742-3747.

(3) Komaguchi, K.; Maruoka, T.; Nakano, H.; Imae, I.; Ooyama, Y.; Harima, Y. *J Phys Chem C* **2010**, *114*, 1240-1245.

(4) Alivisatos, A. P. *J Phys Chem-Us* **1996**, *100*, 13226-13239.

(5) Alivisatos, A. P. *Science* **1996**, *271*, 933-937.

(6) Burda, C.; Chen, X. B.; Narayanan, R.; El-Sayed, M. A. *Chem Rev* **2005**, *105*, 1025-1102.

(7) Murray, C. B.; Kagan, C. R.; Bawendi, M. G. *Annu Rev Mater Sci* **2000**, *30*, 545-610.

(8) Durr, H.; Bossmann, S.; Beuerlein, A. *J Photoch Photobio A* **1993**, *73*, 233-245.

(9) Sato, S.; White, J. M. *Chem Phys Lett* **1980**, *72*, 83-86.

(10) Abe, R.; Sayama, K.; Domen, K.; Arakawa, H. *Chem Phys Lett* **2001**, *344*, 339-344.

(11) Abe, R.; Sayama, K.; Sugihara, H. *J Phys Chem B* **2005**, *109*, 16052-16061.

(12) Zhang, H. Z.; Banfield, J. F. *J Phys Chem B* **2000**, *104*, 3481-3487.

(13) Yu, J. G.; Yu, J. C.; Leung, M. K. P.; Ho, W. K.; Cheng, B.; Zhao, X. J.; Zhao, J. C. *J Catal* **2003**, *217*, 69-78.

Chapter 4

Active Facets on Ti^{3+} Doped TiO_2: An Effective Strategy to Improve the Visible Light Photocatalytic Activity

4.1 Introduction

The properties and applications of materials are significantly controlled by their physical characteristics such as size, shape and structural state. Many processes are governed by interface reactions where the surface energy and reactivity depend on the spatial configuration, coordination and structural state of surface atoms and molecules. For crystals, this dependence is directly related to the expression of specific crystallographic faces which exhibit different surface structures and atomic configurations. These differences explain why some applications, such as molecular adsorption and desorption, gas sensing, drug molecule delivery and release, and heterogeneous catalysis are highly sensitive to the surface atomic structures. Recent progress in the engineering of crystal morphology, has included the synthesis of polyhedral silver nanocrystals by the polyol method;[1] the epitaxially seeded growth of highly faceted Pt-Pd nanocrystals;[2] and the controlled overgrowth of Pd-Au core-shell structures enclosed by facets.[3] Besides these metallic nanocrystals, binary or ternary compounds with preferentially developed facets have also been reported.[4-6]

The facet effect is an important factor for heterogeneous photocatalysts, because surface atom arrangement and coordination intrinsically determine the adsorption of reactant molecules, surface transfer between photoexcited electrons and reactant molecules, and desorption of product molecules.[7] This phenomenon has been well studied in TiO_2 photocatalysts.[8-13] TiO_2 is one of the most extensively studied photocatalysts due to its abundance, nontoxicity, and stability. However, for practical applications, pure TiO_2 is not a good candidate because it is only active under ultraviolet (UV) irradiation due to the band gap of 3.2 eV for the anatase phase. Therefore, band gap engineering is required in order to use TiO_2 as a water-splitting catalyst under visible light irradiation. Reduced TiO_2 (TiO_{2-x}), containing Ti^{3+} or O vacancies has been reported to show visible light absorption.[14,15] Various strategies have been applied to synthesize reduced TiO_2, such as heating under vacuum[16] or reducing gas,[17] laser irradiation,[18] and high energy particle bombardment (electron,[19] or Ar^+ ion[20]). A big challenge for the application of reduced TiO_2 is that the surface oxygen defects are highly unstable in air due to the susceptibility of Ti^{3+} toward O_2.[21] Recently, we reported a facile one-step combustion method to synthesize partially reduced TiO_2.[22] It is found that the presence of Ti^{3+} in the sample extends the photoresponse of TiO_2 from the UV to the visible light region, which leads to high visible light photocatalytic activity for the generation of hydrogen gas from water. However, in the rapid and harsh combustion process, we have

very limited control over the crystallization process, which results in the irregularly shaped products. Here we report the development of a simple solution method to grow non-stoichiometric rutile TiO_2 crystals with desired facets. The incorporation of Ti^{3+}, which extends the light absorption from the UV into the visible, along with the development of facets with high reactivity, results in a material exhibiting greatly enhanced photocatalytic H_2 production activity relative.

4.2 Experimental Section

4.2.1 Synthetic Procedure

All chemicals, including Titanium powder (Aldrich, 99%), and hydrochloric acid (Fisher scientific, 37.1%), were used as received without any further purification.

In a typical synthetic procedure, 0.300 g Titanium powder and hydrochloric acid (2M, 10 mL) were mixed in a 50-mL pyrex beaker and magnetically stirred for 15 minutes. Then the above mixture was transferred to the Teflon-lined stainless-steel autoclave (23 mL capacity) and hydrothermally treated for 12 h under 220 °C. The sample was then collected and washed by distilled water and ethanol for 3 times, respectively.

4.2.2 Characterization

Powder X-ray diffraction data (XRD) were collected using a Bruker D8-Advance powder diffractometer operating at 40kV, 40mA for Cu Kα radiation (λ=1.5406 Å).

The scanning electron microscopy (SEM) images were obtained on Philips XL30 FEG with the accelerating voltage at 10 kv.

Transmission electron microscopy (TEM) was performed with a FEI-Philips CM300 microscope operating at 300 kV accelerating voltage, equipped with a LaB_6 electron gun, and an EDAX energy-dispersive spectrometer (EDS). Samples were prepared by dispersing the unground crystal aggregates in distilled water through ultrasonic agitation and depositing a drop of the resulting suspension onto copper grids

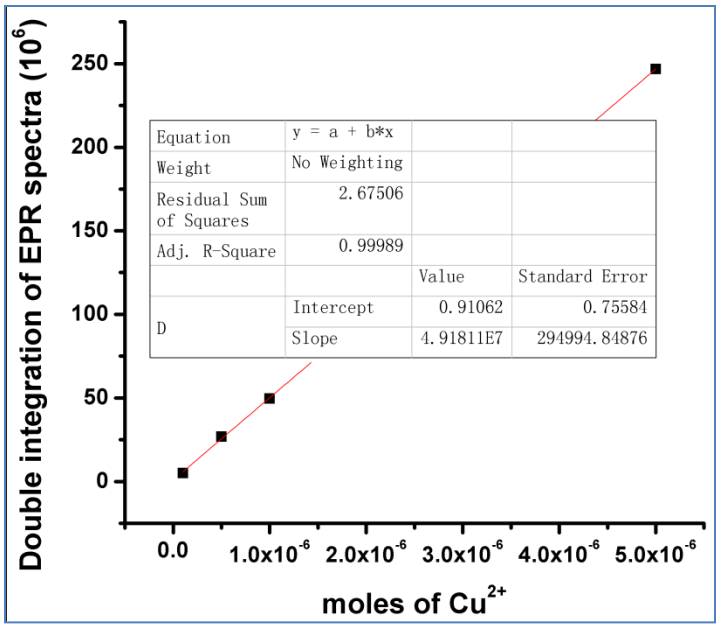

coated with a thin (5 nm thickness) holey carbon support film. Selected-area electron diffraction (SAED) patterns and high-resolution images were obtained from the rutile crystals oriented so that their prismatic faces were normal to the electron beam.

The electron paramagnetic resonance (EPR) spectra were recorded on a Bruker EMX EPR spectrometer at an X-band frequency of 9.363 GHz, sweep width of 500.00 Gauss, and center field of 3390.00 Gauss.

The detailed steps to quatitatively determine the concentration of Ti^{3+} was conducted as follows:

1. We prepared a series of Cu^{2+} aqueous solutions ($CuSO_4 \cdot 5H_2O$ as the salt). The concentrations were 2×10^{-3}M, 1×10^{-2}M, 2×10^{-2}M, and 1×10^{-1}, respectively.
2. We then tested EPR for 50μL of above frozen solution, double integrated the spectra and made a calibration curve, shown below:
3. Finally we measured the EPR for our as-synthesized sample, and used the calibration curve to determine the concentration of Ti^{3+}, which was estimated to be 4.95 μmol/g.

The UV-visible absorption spectra were recorded on a Shimadzu UV-3101PC UV-Vis-NIR spectrophotometer operating in the diffuse mode.

Photocatalytic H_2 production experiments were conducted in a sealed circulation system. 1% Pt was loaded as a cocatalyst by UV irradiation of $PtCl_4$ aqueous solution. In a typical run, 0.100g of sample loaded with Pt was suspended in 120 mL 25% methanol aqueous solution under magnetic stirring. After degassing the system for one hour, a 300 W Xe lamp with a 400 nm cut-on filter (Newport Corp.) was applied to execute the

photocatalytic reaction. The products were analyzed by gas chromatography (Shimadzu GC-8A) equipped with a thermal conductivity detector (TCD).

The external quantum efficiency (EQE) was calculated based on the equation: EQE= 2H/P. Here H was the number of moles of hydrogen gas produced during a specific time, while P was the number of photons incident on the photocatalytic system within the same time period. For measurement of the EQE at 420 nm, a 420 nm bandpass filter (Newport Corp.) was used. The number of the incident photons was determined using a radiant power energy meter (Newport Corp., Model 70260 with a Thermopile Detector).

The sorption isotherms of N_2 were measured by using a Micromeritics ASAP 2020 surface-area and pore-size analyzer.

Time-resolved photoluminescence measurements were made on a 40 kHz Spectra Physics laser system. Some of the 800 nm fundamental beam was frequency doubled to 400 nm, which was then mixed with remaining fundamental to generate the 266 nm pulse used to excite the samples. The per-pulse excitation fluence used was less than 2 $\mu J/cm^2$. Data was collected using a Hammastsu C4334 Streakscope. Glass filters were used to eliminate the scattered pump from the signal. Despite the filters used, some pump scatter did show up in the data at 532 nm as well as some residual 400 nm. These wavelengths were therefore excluded in the time-traces. The samples were packed into an open-face copper sample holder for powders, and kept under vacuum in a Janis ST100 cryostat.

4.3 Results and Discussion

4.3.1 Proposed Reactions

In the hydrothermal condition, we propse that the chemical reaction in the autoclave is as follows:

$$2Ti\ (powder) + 6H^{+} \longrightarrow 2Ti^{3+} + 3H_2$$

$$Ti^{3+} + H_2O \xrightarrow{\Delta} TiOH^{2+} + H^{+}$$

$$TiOH^{2+} \longrightarrow e^{-} + Ti(IV)\ oxo\ species \longrightarrow TiO_2$$

$$TiO_2 + H_2 \longrightarrow TiO_{2-x} + H_2O$$

4.3.2 Structure Characterization

The powder X-Ray diffraction analysis (Figure 1a) shows that the sample of as-produced TiO_2 (S1) has rutile structure. All of the diffraction peaks can be assigned to tetragonal rutile structure with cell parameters a = 4.584 Å and c = 2.953 Å, S.G. $P4_2/mnm$ (JCPDS No. 89-4920). No anatase diffraction peaks are observed. Figure 1b is a typical scanning electron microscopy (SEM) image of the as-synthesized sample. This hydrothermal method produces tetragonal crystals with prismatic habit that are obviously different from the irregular particles we previously prepared (S2, see Figure 2). Based on first principle calculations, the crystal face with the lowest surface free energy for rutile is {110}, a form which is preferentially developed in the crystals from this sample.[23] The high magnification SEM image (Figure 1c) reveals that the rutile crystals are a

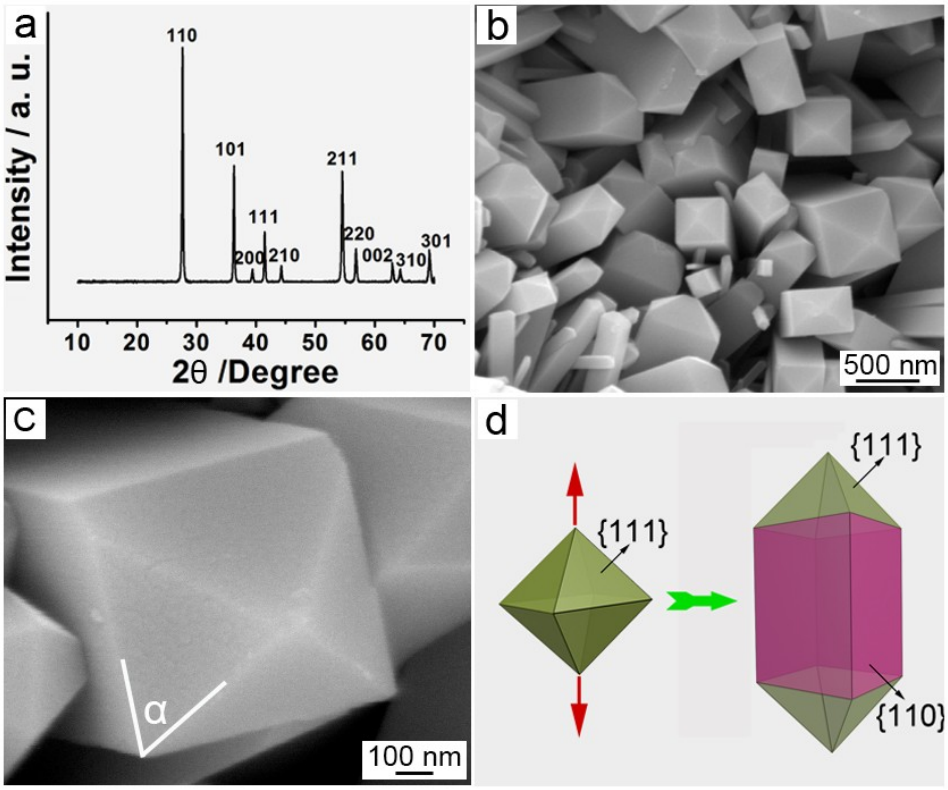

Figure 1. (a) XRD pattern for as-prepared samples through hydro-thermal treatment of Ti powder and HCl under 220 °C for 12 h. (b) Typical SEM image of the rutile crystal, i.e., tetragonal prism with pyramid-like top. (c) High magnification SEM image, showing the top feature of the crystal. (d) Scheme for the faceting of the rutile TiO_2.

combination of prismatic and bipyramidal forms. The angle of 53.6º (∠α) measured between the edges of the prismatic and pyramidal facets (Figure 1c) matches closely the theoretical value between the <110> and <011> directions in a tetragonal lattice with a = 4.584 Å and c = 2.953 Å. From the above investigation, we can propose that the rutile crystals in sample S1 are a combination of {110} tetragonal prism and {111} tetragonal bipyramid, with preferentially developed {110} prismatic faces, which gives the crystals

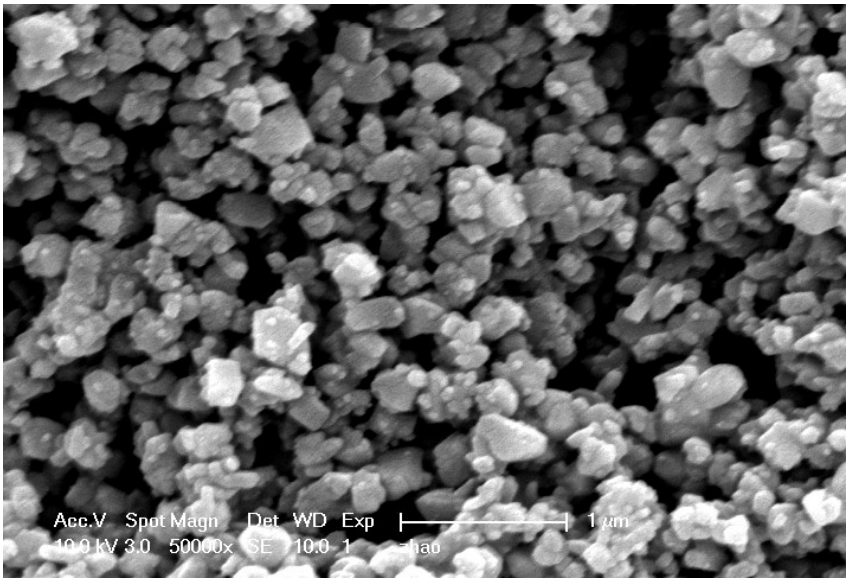

Figure 2. A typical SEM image for the sample synthesized from previous reported combustion method, i.e. combustion in air of the ethanol solution of Titanium (IV) isopropoxide and 2-ethylimidazole at 500 °C and kept in the oven for 5 hours.

elongated habit along the c axis (Figure 1d). This interpretation is unambiguously proven by transmission electron microscopy (TEM) characterization. Figure 3a shows a TEM image of a representative rutile single crystal, and the corresponding selected area electron diffraction (SAED) pattern, which is overlaid on top of the crystal image. The spot SAED pattern clearly demonstrates the single crystal nature of the individual grains of this sample. The SEAD pattern was taken with the electron beam normal to one of the prismatic faces of the crystal. Inspection of the indexed [110] zone axis pattern reveals that the prismatic crystal faces are parallel to {110}, the bipyramid faces are parallel to {111} and the elongation of the crystal is parallel to <001>. This is confirmed by the high

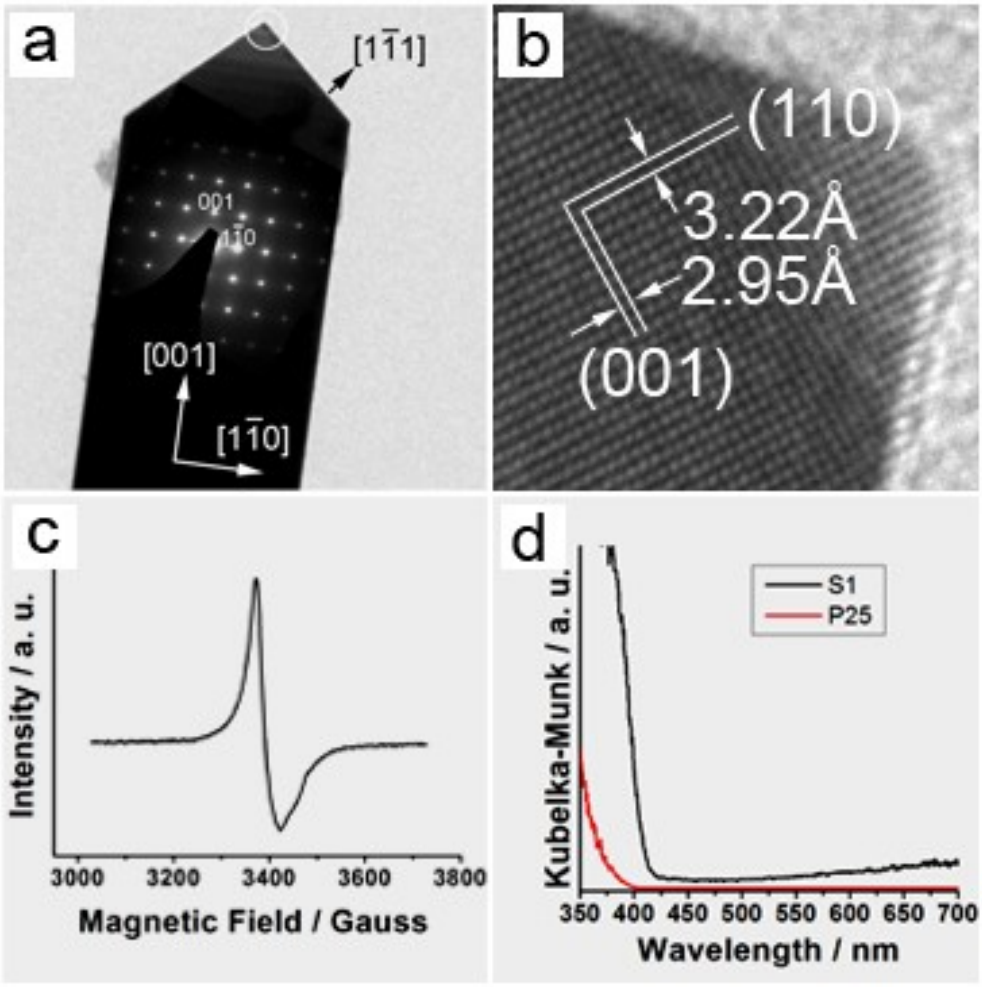

Figure 3. (a) Typical TEM image for rutile TiO_2 single crystal. The overlaid inset is the oriented [110] SAED pattern from this crystal. (b) High resolution TEM image taken from the marked area in Figure 3a. (c) EPR spectra measured at 100K. (d) UV-visible diffuse reflectance spectra for commercial P25 (dotted line) and S1 (solid line).

resolution TEM (HRTEM) image taken from the marked area in the low magnification TEM image (Figure 3b), which reveals the crystal lattice and the orientation of the lattice planes with respect to the crystal faces. The lattice fringes of 3.22 Å and 2.95 Å,

correspond to the {110} and {001} lattice spacing respectively, corroborating the SAED measurements.

4.3.3 EPR Examination

Electron paramagnetic spectra (EPR) were recorded under 100K to determine the presence of Ti^{3+}. A strong EPR signal shows up at g = 1.97 in Figure 3c, which could be

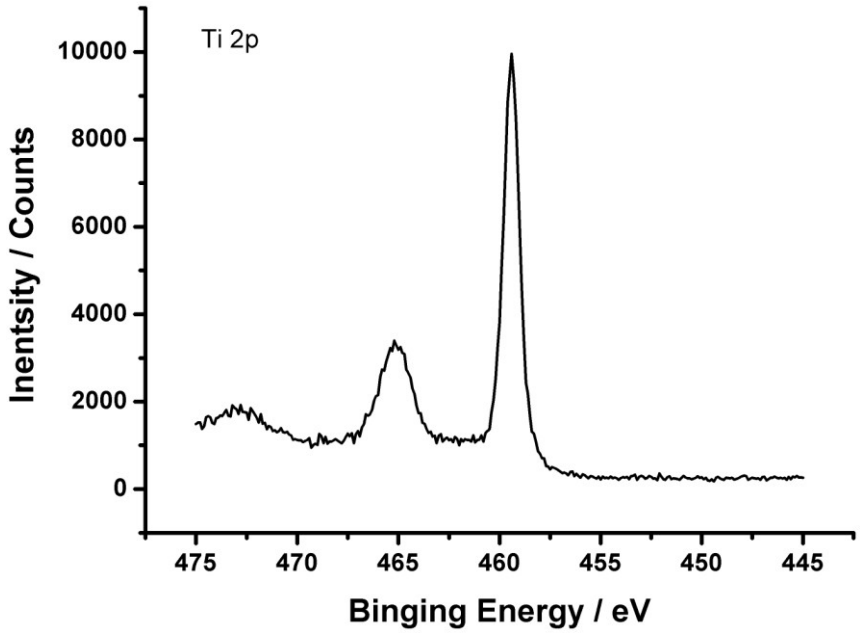

Figure 4. The Ti 2p XPS spectra of the as-synthesized S1. No Ti^{3+} signal (at 456.6 eV) was detected.

assigned to Ti^{3+},[24] thus proving the existence of the Ti^{3+} in the synthesized sample (Figure 3c). The presence of Ti^{3+} may result from reduction of Ti^{4+} by H_2, which is produced by the reaction between Ti powder and HCl, and the details are presented in Supporting Information. It is worth noting that the EPR spectra also excludes the presence of Ti^{3+} on

the surface of the sample since the surface Ti^{3+} is prone to adsorb atmospheric O_2, which would be reduced to O_2^- and will show an EPR signal at $g \approx 2.02$,[25] which is absent in our spectrum. The XPS study further confirmed that no Ti^{3+} exist on the surface (Figure 4). Having all of the Ti^{3+} located in the bulk is crucial for the stability of our non-stoichiometric TiO_2 sample, since the surface oxygen defects are usually not stable enough to survive in air and are even susceptible to oxidation by dissolved oxygen in water.[21,26] The concentration of Ti^{3+} was determined by numerical double integration of EPR spectra and comparison with a frozen aqueous solution of Cu^{2+}. Here the concentration of Ti^{3+} was estimated to be 4.95 μmol/g. The absolute accuracy was approximate ± 20%.[27]

4.3.4 UV-visible absorption

Figure 3d shows the UV-visible absorption spectra for sample and the commercial Dequssa P25 (a mixture of anatase and rutile TiO_2). Compared to the stoichiometric TiO_2, the partially reduced sample shows a red shift in the spectrum, suggesting a decrease in the band gap. Our calculation has demonstrated that the Ti^{3+} inside the bulk TiO_2 could induce a vacancy band of electronic states just below the conduction band, which is responsible for the band gap narrowing.[22] The assumption of a miniband also explains why the absorbance in the visible range for the as-prepared sample is stronger than that for Ti^{3+} free P25.

4.3.5 H_2 Evolution

The photocatalytic activity of the sample for hydrogen production from water was tested. After loading 0.100 g sample with 1% Pt (0.001 g), the photocatalyst S1 was

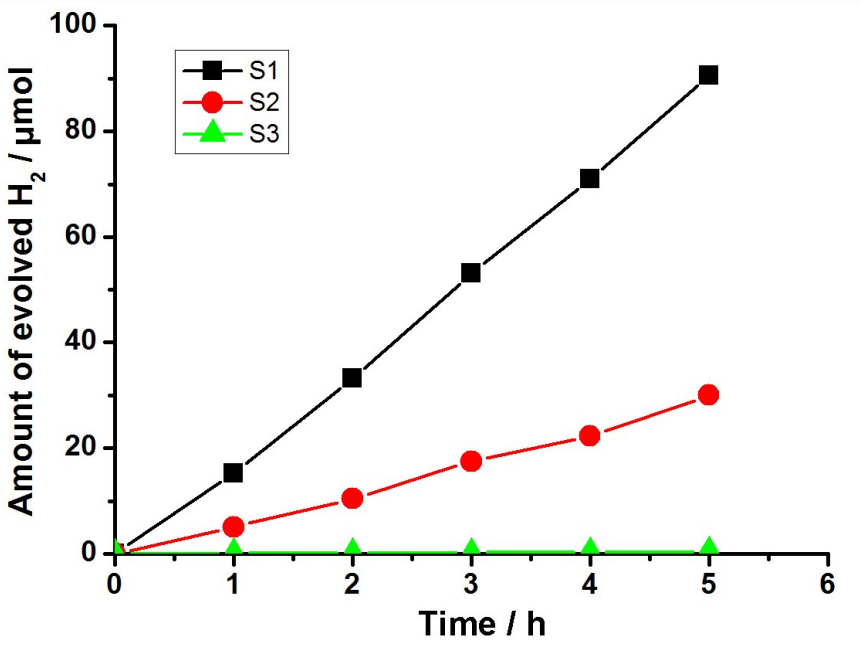

Figure 5. Time course of evolved H_2 under visible light (>400 nm) illumination. (■) Sample S1, reduced TiO_2, tetragonal prism; (●) Sample S2, reduced TiO_2, irregular nanoparticles; (▲) Sample S3, stoichiometric TiO_2, tetragonal prism.

placed into a 120 mL 25% methanol aqueous solution in a closed-gas circulation system. A Xe lamp (300 W) with a 400 nm cut-on filter was used to cut off the UV light and allow only visible light (>400 nm) to go through. Figure 5 shows the time course of H_2 evolution for as-prepared sample S1. Under the above reaction conditions, the sample could steadily produce hydrogen gas at ~ 18.1 µmol/h/0.100g. After illumination for 100 h, 1843 µmol H_2 was evolved in total, accounting for a turnover number of 1.47. This

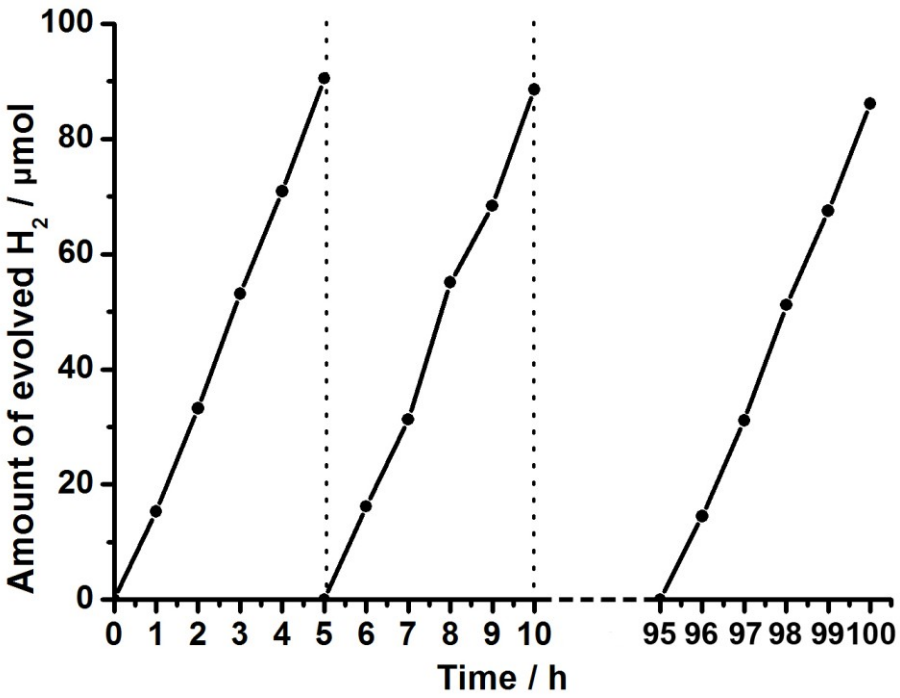

Figure 6. Time course of evolved H_2 under visible light (>400 nm) irradiation. (a) Reaction for 5 h; (b) system evacuated and reaction continued for another 5 h; (c) after illumination for 95 h, system evacuated and the reaction continued for another 5h.

result proves the H_2 production is a photocatalytic process. Note that no noticeable decrease in H_2 production rate was observed within the 100 h photocatalytic period (Figure 6), demonstrating the high stability of the photocatalyst. We measured the external quantum efficiency (EQE) with a 420 nm band pass filter, which gave an EQE of 2.28%.

4.3.6 Facet Effect

The effect of the active facets is investigated by comparing sample S1 with our previously reported reduced TiO_2 irregular nanoparticles S2. Under the same

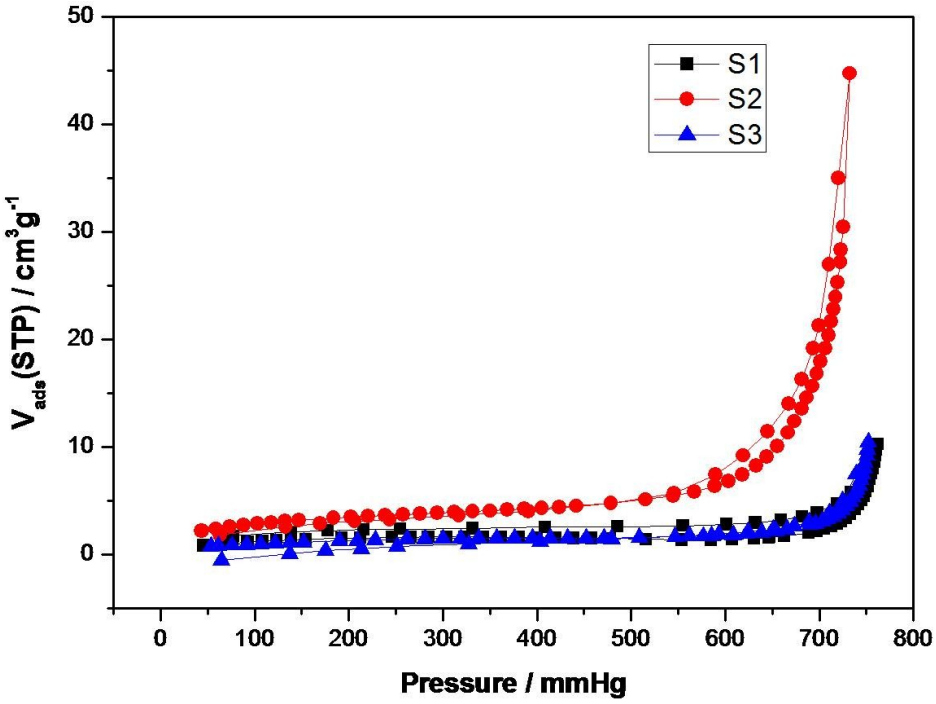

Figure 7. The N_2 adsorption/desorption isotherms at 77 K.

photoreaction conditions, the S1 exhibits 200% improvement (18.1 µmol/h/0.100g vs 6.0µmol/h/0.100g), which strongly demonstrates the enhancement of the photocatalytic activity owing to the active facets. We have measured the surface area of these samples and find that S1 has a much lower surface area than S2 (5.5 m^2 g^{-1} vs 11.7 m^2 g^{-1}) even though its activity is much higher. This decrease in surface area would be expected to lower S1's catalytic activity, contrary to what is observed. Thus the increased activity of S1 must result from some other feature of its morphology. It has been reported that {111} and {110} facets are prone to collect holes and electrons, respectively,[28,29] which greatly improves the separation of holes and electrons. SEM imaging of sample S1 after the photocatalytic reaction (Figure 8) revealed that no deformation or size and shape

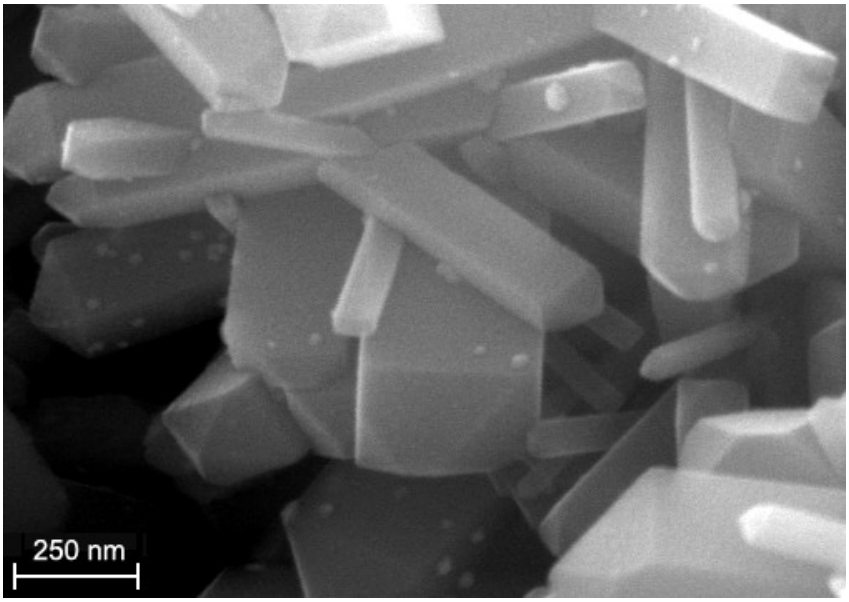

Figure 8. Representative SEM image of the sample S1 after photocatalytic reaction, showing the Pt nanoparticles (white spots).

changes have taken place during the photocatalytic reaction. Of greater importance is the observation that the Pt nanoparticles accumulated exclusively on the {110} facets, without any Pt nanoparticles found on the {111} facets. This observation proves that the photogenerated electrons selectively gathered on the {110} facets, where the Pt (IV) was reduced to Pt nanoparticles. In order to further examine how the shape of the particle influences the electron-hole dynamics, we compared the fluorescence decays from samples S1 and S2. Both samples show the highly nonexponential decay of fluorescence centered around 480 nm that has previously been attributed to surface trap states.[30] The distribution of surface traps, with different lifetimes, is what leads to the highly nonexponential decays. But in S1, where the {111} and {110} facets are

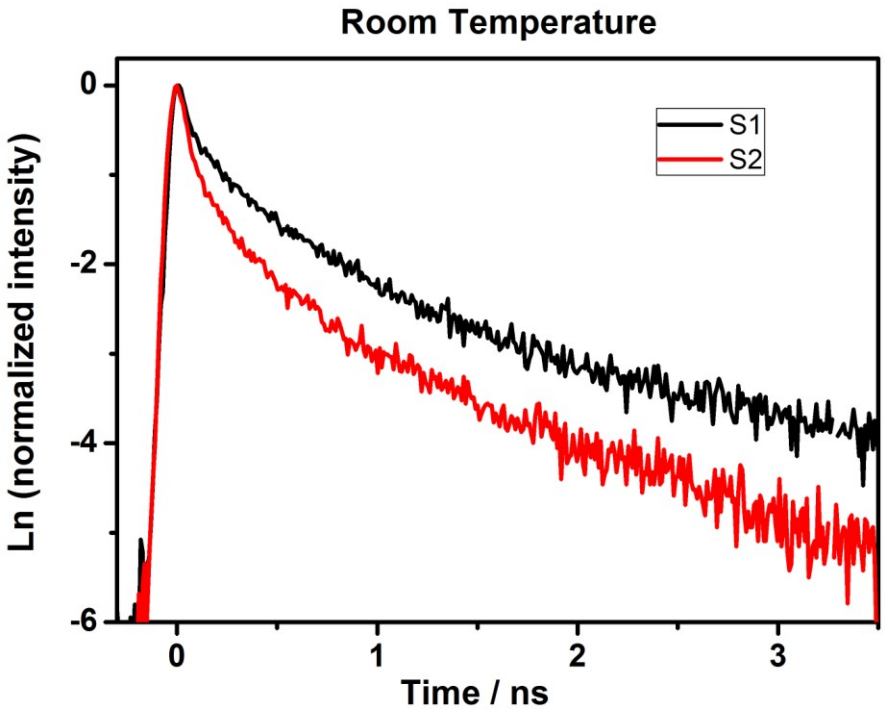

Figure 9. The time-resolved photoluminescence measurement for tetragonal prism S1 (black), and irregular nanoparticle S2 (red) at room temperature.

well-defined, the fluorescence lifetime is significantly longer than in the irregularly shaped S2 sample. Although we cannot extract a single decay time, the 1/e decay time is almost twice as long for the S1 sample at room temperature as seen from Figure 9. This difference becomes more pronounced at lower temperatures, as shown in Figure 10. At 84 K, the S1 1/e decay time is almost 4 times longer, and it is clear that the short-time decay in S2 is much reduced in S1. If we attribute the fluorescence decay to recombination of the surface trapped electron or hole with its counterpart, then it appears that rapid recombination events play a smaller role in S1. If electrons and holes are trapped at

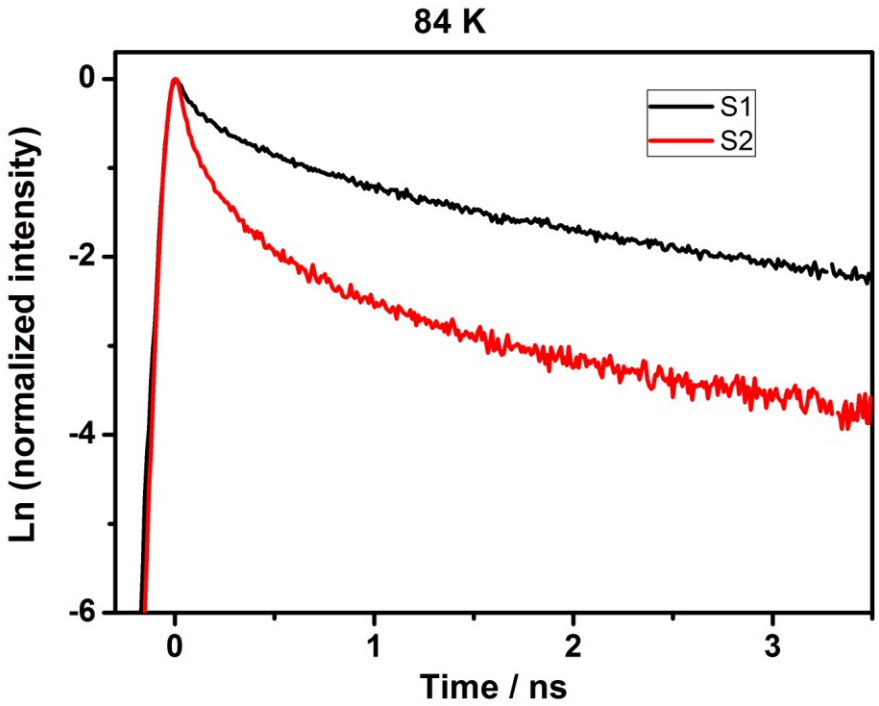

Figure 10. The time-resolved photoluminescence measurement for tetragonal prism S1 (black), and irregular nanoparticle S2 (red) at 84 K.

crystallographically different crystal facets, such as the {111} and {110} in the S1 sample, then this effective separation of the electron and hole would suppress rapid recombination events, as observed experimentally. Slower electron-hole recombination would provide the trapped charges with more opportunities to initiate surface reactions, presumably enhancing the photocatalytic activity as observed for these particles as well. We also ran a control experiment on a stoichiometric rutile TiO_2 sample with active facets (sample S3) formed by heating S1 in air under 210 °C for 8h. After oxidation, S3 retains the original prismatic shape of the S1 sample (Figure 11) but almost completely loses its photocatalytic activity (<0.1 μmol/h/0.100g). EPR measurements show no presence of

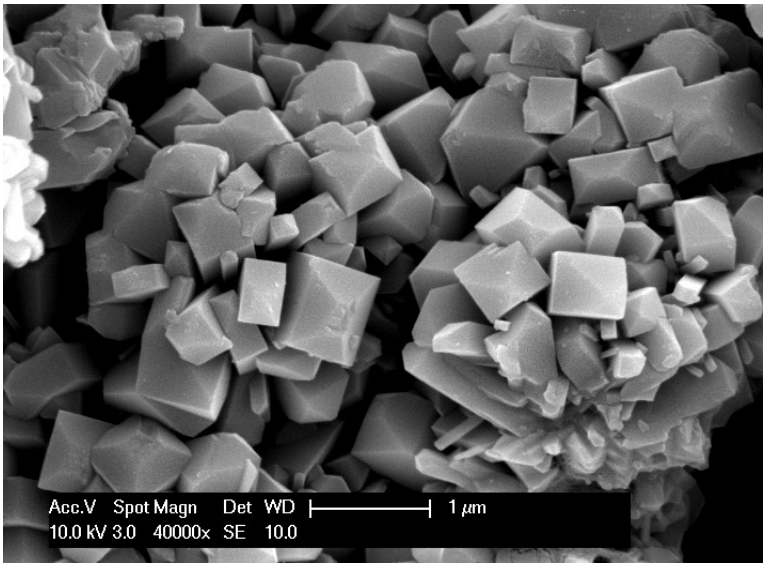

Figure 11. The SEM image for the stoichimetric sample S3 by post treating the S1 in air for 8h at 210°C.

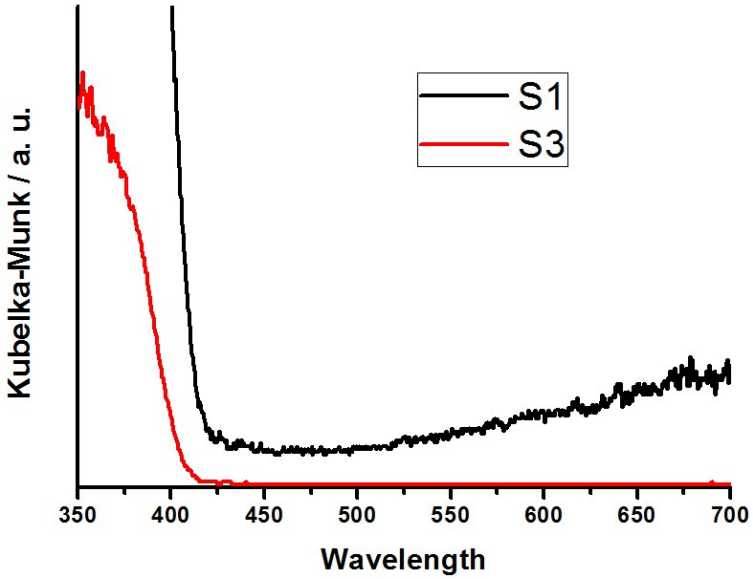

Figure 12. The UV-visible diffuse reflectance spectra for S1 and stoichiometric sample S3 by post treating the S1 in air for 8h at 210°C.

Ti^{3+} in the S3, and the UV-vis spectra reveal that the absorbance of visible light (wavelength greater than 400 nm) is nearly extinguished (Figure 12). This control

experiment demonstrates that it is the Ti^{3+} that effectively extends the photo response of TiO_2 from UV to visible light region, resulting in the visible light activity of the as-synthesized S1.

4.4 Conclusion

We have synthesized a partially reduced non-stoichiometric rutile TiO_2 with active facets by a facile solution method. This highly stable photocatalytic material has a greatly improved efficiency to reduce water when compared to irregularly shaped nanoparticles. The new synthetic approach presented here provides a way to control the final crystal morphology of the target product. We expect to utilize this new strategy to explore how the interplay of chemical composition and nanoscale morphology

4.5 References

(1) Tao, A.; Sinsermsuksakul, P.; Yang, P. D. *Angew Chem Int Edit* **2006**, *45*, 4597-4601.

(2) Habas, S. E.; Lee, H.; Radmilovic, V.; Somorjai, G. A.; Yang, P. *Nat Mater* **2007**, *6*, 692-697.

(3) Lim, B.; Kobayashi, H.; Yu, T.; Wang, J. G.; Kim, M. J.; Li, Z. Y.; Rycenga, M.; Xia, Y. N. *J Am Chem Soc* **2010**, *132*, 2506-2507.

(4) Sadtler, B.; Demchenko, D. O.; Zheng, H.; Hughes, S. M.; Merkle, M. G.; Dahmen, U.; Wang, L. W.; Alivisatos, A. P. *J Am Chem Soc* **2009**, *131*, 5285-5293.

(5) Bi, Y.; Ouyang, S.; Umezawa, N.; Cao, J.; Ye, J. *J Am Chem Soc* **2011**, *133*, 6490-6492.

(6) Xi, G. C.; Ye, J. H. *Chem Commun* **2010**, *46*, 1893-1895.

(7) Liu, G.; Yu, J. C.; Lu, G. Q.; Cheng, H. M. *Chem Commun* **2011**, *47*, 6763-6783.

(8) Yang, H. G.; Sun, C. H.; Qiao, S. Z.; Zou, J.; Liu, G.; Smith, S. C.; Cheng, H. M.; Lu, G. Q. *Nature* **2008**, *453*, 638-642.

(9) Liu, G.; Yang, H. G.; Wang, X. W.; Cheng, L. N.; Pan, J.; Lu, G. Q.; Cheng, H. M. *J Am Chem Soc* **2009**, *131*, 12868-12869.

(10) Liu, G.; Sun, C. H.; Yang, H. G.; Smith, S. C.; Wang, L. Z.; Lu, G. Q.; Cheng, H. M. *Chem Commun* **2010**, *46*, 755-757.

(11) Pan, J.; Liu, G.; Lu, G. M.; Cheng, H. M. *Angew Chem Int Edit* **2011**, *50*, 2133-2137.

(12) D'Arienzo, M.; Carbajo, J.; Bahamonde, A.; Crippa, M.; Polizzi, S.; Scotti, R.; Wahba, L.; Morazzoni, F. *J Am Chem Soc* **2011**, *133*, 17652-17661.

(13) Hosono, E.; Fujihara, S.; Kakiuchi, K.; Imai, H. *J Am Chem Soc* **2004**, *126*, 7790-7791.

(14) Iyengar, R. D.; Codell, M. *Adv Colloid Interfac* **1972**, *3*, 365-388.

(15) Cronemeyer, D. C. *Phys Rev* **1959**, *113*, 1222-1226.

(16) Serwicka, E. *Colloid Surface* **1985**, *13*, 287-293.

(17) Wang, G. M.; Wang, H. Y.; Ling, Y. C.; Tang, Y. C.; Yang, X. Y.; Fitzmorris, R. C.; Wang, C. C.; Zhang, J. Z.; Li, Y. *Nano Lett* **2011**, *11*, 3026-3033.

(18) Ohtsu, N.; Kodama, K.; Kitagawa, K.; Wagatsuma, K. *Appl Surf Sci* **2010**, *256*, 4522-4526.

(19) Kimmel, G. A.; Petrik, N. G. *Phys Rev Lett* **2008**, *100*.

(20) Hashimoto, S.; Tanaka, A. *Surf Interface Anal* **2002**, *34*, 262-265.

(21) Teleki, A.; Pratsinis, S. E. *Phys Chem Chem Phys* **2009**, *11*, 3742-3747.

(22) Zuo, F.; Wang, L.; Wu, T.; Zhang, Z. Y.; Borchardt, D.; Feng, P. Y. *J Am Chem Soc* **2010**, *132*, 11856-11857.

(23) Barnard, A. S.; Curtiss, L. A. *Nano Lett* **2005**, *5*, 1261-1266.

(24) Conesa, J. C.; Soria, J. *J Phys Chem-Us* **1982**, *86*, 1392-1395.

(25) Anpo, M.; Che, M.; Fubini, B.; Garrone, E.; Giamello, E.; Paganini, M. C. *Top Catal* **1999**, *8*, 189-198.

(26) Komaguchi, K.; Maruoka, T.; Nakano, H.; Imae, I.; Ooyama, Y.; Harima, Y. *J Phys Chem C* **2010**, *114*, 1240-1245.

(27) Howe, R. F.; Gratzel, M. *J Phys Chem-Us* **1985**, *89*, 4495-4499.

(28) Ohno, T.; Sarukawa, K.; Matsumura, M. *New J Chem* **2002**, *26*, 1167-1170.

(29) Bae, E.; Murakami, N.; Ohno, T. *J Mol Catal a-Chem* **2009**, *300*, 72-79.

(30) Fujihara, K.; *et al. J Photoch Photobio A* **2000**, *132*, 99-104.